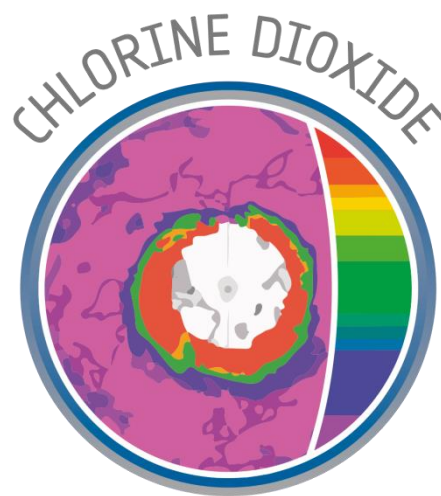# Monitoring Stratospheric OClO with Sentinel-5p (S5pOClO)

Sentinel-5p + Innovation - Theme 2: Chlorine Dioxide

Algorithm Theoretical Baseline Document

document number	:	S5p+I_OCLO_IUP-UB_ATBD
authors	:	Andreas Meier, Andreas Richter, Gaia Pinardi, Christophe Lerot
distributed to	:	Christian Retscher
issue	:	3.0
date	:	2023-08-15
status	:	Final

Contents

1   List of Figures

2   List of Tables

3 Purpose and objective

The present document is the Algorithm Theoretical Basis Document (ATBD) for the Sentinel 5 Precursor (S5p) Level 2 (L2) algorithm that will deliver chlorine dioxide (OClO) column amounts. The purpose of the ATBD is to provide the theoretical basis for the algorithm and to describe the necessary input and auxiliary data, as well as the output that will be generated. In addition, information about the expected size of the product, expected calculation times, and the expected accuracy are provided.

4 Document overview

The outline of the document is as follows. Section 5 introduces references, terms and acronyms used. Sections 6 and 7 generally describe the importance of chlorine dioxide and its retrieval from remote sensing instruments

5 References, terms and acronyms

Terms, symbols and abbreviations that are used within the Sentinel 5p Level-2 project are described in [RD01]. Terms, symbols and abbreviations that are specific for this document can be found below.

5.1 References

5.1.1 Applicable documents

[AD01] Sentinel-5p Innovation (S5p+I) - Statement of Work - EOP-SD-SOW-2018-049
   source: ESA, **issue**: 2, **date**: 2018-08-20
[AD02] Sentinel-5p + Innovation -Theme 2: Chlorine Dioxide, Monitoring Stratospheric OClO with Sentinel-5p (S5pOClO), Requirement Baseline Document
   source: IUP-UB, **ref**: S5p+I_OCLO_IUP-UB_RB, **issue**:1.0, **date**: 2019-11-01

5.1.2 Reference documents

[RD01] Terms, and symbols in the TROPOMI Algorithm Team
   source: KNMI; **ref**: SN-TROPOMI-KNMI-L2-049-MA; **issue**: 1.0.0; **date**: 2015-07-16
[RD02] TROPOMI Instrument and Performance Overview.
   source: KNMI; **ref**: S5p-KNMI-L2-0010-RP; **issue**: 0.10.0; **date**: 2014-03-15
[RD03] [AD5] Sentinel-5p+Innovation: Theme 2; Monitoring Stratospheric OClO with Sentinel-5p (S5pOClO): Validation Report.
   Source: BIRA-IASB, **issue:** 2.0, **ref:** S5p+I_OCLO_BIRA_VR, **date:** 15/08/2023.
[RD04] [AD5] Sentinel-5p+Innovation: Theme 2; Monitoring Stratospheric OClO with Sentinel-5p (S5pOClO): Product User Manual.
   Source: IUP-UB, **issue:** 1.0, **ref:** S5p+I_OCLO_IUP-UB_PUM, **date:** 15/08/2023.

5.2 Terms, definitions and abbreviated terms

Term	Symbol	Definition
hyperspectral imager		imager with a large number of spectral channels, often at high spectral resolution (better than about 0.5-1 nm), e.g. GOME-2, SCIAMACHY
imaging spectrometer		spectrometer that images the entrance slit on a two-dimensional CCD detector having wavelength on one axis and along-slit position on the other axis, e.g. OMI or TROPOMI
columns of the CCD		different columns correspond to different wavelengths in TROPOMI
rows of the CCD		different rows correspond to different across-track viewing directions in TROPOMI
box air mass factors	$\mathbf{m}$, m_l	box air mass factors (column vector), l-th element is box air mass factor for model layer l
air mass factor	M	column or total air mass factor
number concentration	n(z)	in units of m^{-3}
vertical column	N_v	in units of mol m^{-2}
slant column	N_s	
processing flag		A processing flag is understood to be binary; a technical processing flag is raised in case of processing errors (failures) or processing warnings.

ATBD	Algorithm Theoretical Base Document
CTM	Chemistry Transport Model
DOAS	Differential Optical Absorption Spectroscopy
ENVISAT	Environmental Satellite
EO	Earth Observation
ESA	European Space Agency
GOME	Global Ozone Monitoring Experiment
IASB-BIRA	Royal Belgian Institute for Space Aeronomy
ISRF	Instrument Spectral Response Function

IUP-UB	Institute of Environmental Physics (Institut für Umweltphysik), University of Bremen
OMI	Ozone Monitoring Instrument
RTM	Radiative Transfer Model
SZA	Solar Zenith Angle
S-3, -4, -5, -5p	Sentinel-3, -4, -5, -5-precursor
SCIAMACHY	Scanning Imaging Absorption Spectrometers for Atmospheric Chartography
TOA	Top of atmosphere
TROPOMI	TROPOspheric Monitoring Instrument

6 TROPOMI instrument description

A description of the TROPOMI instrument and performance, referred to from all ATBDs, can be found in [AD01].

7 Introduction to the TROPOMI product

7.1 TROPOMI onboard Sentinel-5p

The TROPOspheric Monitoring Instrument (TROPOMI) (Veefkind et al., 2012) is the only satellite sensor on board of the Copernicus Sentinel-5 Precursor satellite. TROPOMI on S5p is a spectrometer with spectral bands in the ultraviolet (UV), the visible (VIS), the near-infrared (NIR) and the shortwave infrared (SWIR). TROPOMI is a nadir-viewing hyperspectral imager with the purpose of measurement of atmospheric properties and constituents, in particular in the troposphere. The instrument uses passive remote sensing techniques to measure the top of the atmosphere radiation scattered and reflected from the Earth's surface and atmosphere. In addition, a solar irradiance measurement is taken once per day. Light from the entire swath is recorded simultaneously and dispersed onto two-dimensional imaging detectors. The instrument operates in a push-broom configuration with a wide swath enabling nearly daily global observation of backscattered sunlight from the UV into the blue spectrum (280 nm to 500nm imaged by four separate spectrometers), from 675 to 775 nm in the red to NIR (imaged by another two separate spectrometers), with additional measurements taken in the SWIR. The two dimensional detectors enable a nominal ground pixel size of 3.5 x 7 km^2 for the UV/visible part of the spectrum at wavelengths >300 nm. Analysis of measurements taken during the first year of TROPOMI observations showed that the obtained spectra have a very good signal to noise ratio and are rather stable over time. Hence it was decided to further improve the spatial resolution of the UV/visible channels to 3.5 x 5.5 km^2 from August 2019 onwards.

7.2 Background

An important issue in atmospheric science remains the understanding of the stratospheric ozone (O$_3$) depletion and its response to environmental policy. Monitoring of ozone is essential as it shields Earth's surface from harmful UV radiation. Ozone also plays a critical role in many chemical processes

occurring in the atmosphere and contributes to global warming both directly and indirectly. In the stratosphere, ozone loss rates are determined by the concentrations of active chlorine, bromine, nitrogen and hydrogen oxides present in the atmosphere. This is especially relevant in Polar Regions, where low temperatures in winter and spring favour heterogeneous activation of chlorine reservoirs.

A key question related to the expected recovery of stratospheric ozone is the degree of chlorine activation observed in polar winter and spring in both hemispheres. This effect depends not only on the total available inorganic chlorine but also on the presence of polar stratospheric clouds (PSC). Reservoir chlorine species of primarily anthropogenic origin are converted to chlorine radicals or their precursors by means of heterogeneous reactions taking place on the surface of PSC particles. The temperature threshold for the formation of PSCs is about 195 K and hence they can usually only be observed in the wintertime polar stratosphere. The increased concentration of greenhouse gases has an impact on temperatures also in the stratosphere, where lower temperatures are expected for a high CO_2 future. Stratospheric dynamics are relevant for the stability of the Polar Vortex and thus affect the effectiveness of the chemical reactions taking place. Differences in stratospheric dynamics explain both inter-annual variability of ozone depletion and the differences between the two hemispheres. Future changes in atmospheric dynamics will affect the speed of stratospheric ozone recovery.

One good indicator for chlorine activation is the presence of OClO, which is formed by reaction of Bromine Oxide (BrO) and Chlorine Oxide (ClO). In spring, photolysis releases the chlorine radicals initiating the catalytic destruction of ozone resulting in the so-called ozone hole over the springtime poles. Within this context, the ClO-BrO-cycle is an efficient ozone destruction mechanism in the lower polar stratosphere. Although OClO does not participate directly in the destruction of ozone, its accurate measurement as well as modelling is crucial to understand the highly perturbed chlorine chemistry in the polar vortices. While almost no OClO is found outside the Polar Vortex and during warm winters in the Northern Hemisphere, large OClO columns are observed during the winter / spring periods in the SH Polar Vortex and also the NH Polar Vortex during cold winters.

Model predictions still differ significantly from the measured quantities. OClO amounts are underestimated for conditions of strong chlorine activation and at large solar zenith angles. OClO cannot be adequately reproduced within the range of uncertainties given for the various model parameters.

7.3   Heritage

Halogen oxides such as BrO, OClO, and IO have structured absorption cross-sections in the UV and visible part of the spectrum, which can be used to detect and quantify their atmospheric abundances using the Differential Optical Absorption Spectroscopy (DOAS) method. This method has originally been developed and applied for ground-based observations, but was later extended to air-borne and satellite-borne measurements.

For OClO, the first detection from the ground was reported by Solomon et al., (1988) in Antarctica, and subsequently by many other measurements in both hemispheres (Gil et al., 1996; Kreher et al., 1996; Richter et al., 1999; Tørnkvist et al., 2002). Observations from aircraft (Schiller et al., 1990)

followed during AASE campaigns and from balloons in Pommereau and Piquard, (1994) and Renard et al., (1997).

The first retrievals on Global Ozone Monitoring Experiment (GOME) satellite data were presented by Wagner et al., (2001, 2002), Burrows et al., (1999) and Richter et al., (2005), followed by application to measurements of the Scanning Imaging Spectrometer for Atmospheric Chartography (SCIAMACHY) (Oetjen et al., 2011), GOME-2 and the Ozone Monitoring Instrument (OMI). In addition to these nadir viewing observations, OClO was also detected in limb measurements from SCIAMACHY (Kühl et al., 2008) and OSIRIS (Krecl et al., 2006) as well as in stellar occultation measurements from the Global Ozone Monitoring by Occultation of Stars (GOMOS) instrument (Fussen et al., 2006). Outside the Polar Vortex, OClO was detected in volcanic plumes, both from aircraft (General et al., 2015) and from satellite (Theys et al., 2014).

7.4 Requirements

The scientific requirements for the S5p OClO product are mainly determined by the need to monitor stratospheric chlorine activation over time in order to document the continuing effectiveness of the measures taken in the Montreal Protocol and its amendments. Recent reports of unexpected emissions of CFCs (Rigby et al., 2019) underline the relevance of such monitoring. While OClO observations do not provide a direct measure of stratospheric chlorine concentrations, they are an indicator of stratospheric chlorine activation. For long-term stratospheric monitoring, the most important aspect of the OClO data set is its internal consistency in order to draw reliable conclusions on long-term atmospheric changes.

For scientific applications outside of polar stratospheric ozone research such as detection of OClO in lee waves or volcanic emissions, the scientific requirements are mainly the avoidance of false positive detection in the presence of aerosols, clouds and temperature changes and a low noise.

To the knowledge of the authors, no operational thresholds or relative uncertainty requirements have been defined for OClO slant columns for any instrument so far. For the AC SAF OClO GOME2 product, there were general requirements: threshold accuracy of 100%, target accuracy of 50% and optimal accuracy of 30%. Typical OClO slant columns observed at 90° SZA in the fully activated vortex are of the order of 2×10^{14} molec cm^{-2}. For GOME2, standard deviations of 6×10^{13} molec cm^{-2} are found for individual measurements and systematic differences between the different GOME instruments of the order of $1-2 \times 10^{13}$ molec cm^{-2} (Richter et al., 2009, 2016). Similar if not better values should be achieved with the S5p OClO retrievals.

8 Algorithm description

8.1 Overview

The basic structure of the S5p chlorine dioxide algorithm with its most important data fields is illustrated in Figure 8.1. The main data flow is indicated in green. The algorithm consists of two

processing modules, which are indicated in red. Auxiliary input or additional output fields are shown in light blue for static data and dark blue for dynamic data.

Earth radiance spectra and the daily solar irradiance measurement (L1 spectra) are read by the DOAS module, which performs the spectral fit and yields slant column densities (SCDs). Auxiliary inputs for the spectral fit are the absorption cross-sections for chlorine dioxide, other trace gases and so-called pseudo-absorbers, as well as a high-sampling solar irradiance reference spectrum (Fraunhofer atlas). Absorption cross-sections either have to be convoluted to the resolution of S5p or are provided at high spectral resolution for convolution with the instrument spectral response function (ISRF) in the retrieval. Details of the DOAS module are described in section 8.2

Before slant columns are used, an offset correction may have to be applied in the post-processing module POST. The offset correction is applied by calculating mean (or median) chlorine dioxide values over a selected region expected to have very low chlorine dioxide columns (e.g. the equatorial Pacific). These values are then subtracted from all slant columns. The correction is done by across-track viewing direction, and thus implicitly includes a de-striping of fitted slant columns. Striping is a well-known problem of imaging detectors and usually corrected for in an empirical manner (Boersma et al., 2004). Details of the destriping in the POST module can be found in section 8.3.

A top-level summary of the OClO retrieval is given in Table 8.1.
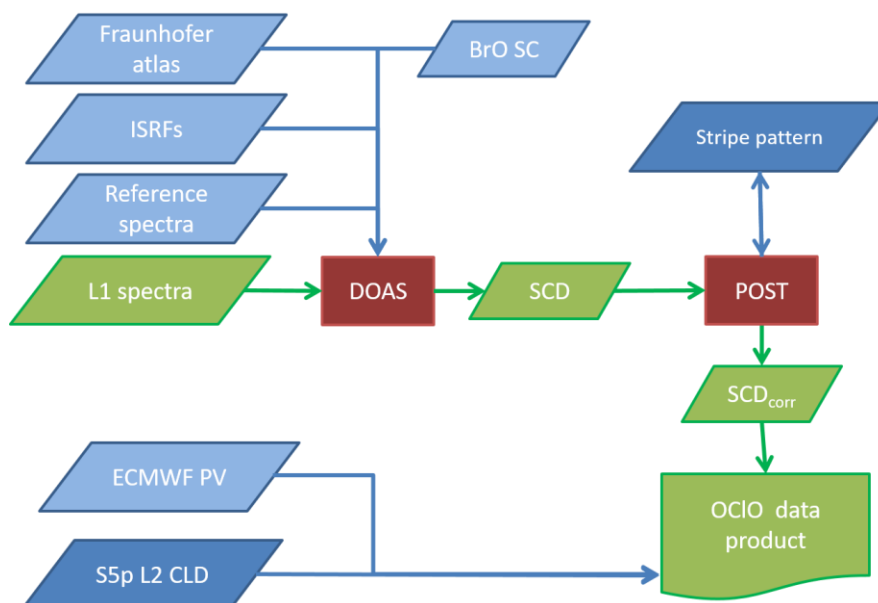
Figure 8.1: The basic structure of the S5p chlorine dioxide algorithm with its most important data fields. The main data flow is indicated in green. The algorithm consists of two processing modules, which are indicated in red. Auxiliary input or additional output fields are shown in blue (light blue for static data and dark blue for dynamic data). The two modules are described in detail in Sections 8.2 and 8.3.

Table 8.1: Overview on the S5P OClO algorithm settings

Analysis details	TROPOMI OClO v0.97
Analysis window	345-389nm
Cross-sections	See Table 8.2
Polynomial	5. Order (6 coeffs.)
Additive polynomial	offset and slope
Background spectrum	Daily irradiance
Post-processing	Destriping, offset correction

8.2 Spectral fit (DOAS)

8.2.1 Approach

The spectral fit in the chlorine dioxide retrieval follows the well-known DOAS approach, which basically applies Lambert Beer's law to the extinction in the atmosphere. The fundamental idea is to separate the problem of column retrieval into two parts:

- The spectroscopic detection and quantification of the number of chlorine dioxide molecules along the light path per unit area, and
- the calculation of the length of the light path.

The first step of the problem is solved by assuming that the total extinction can be separated into two parts: The extinction by scattering which is smooth in wavelength, and the absorption by trace gases which has structured spectral features. With this separation, the measurement can be expressed as the so called DOAS equation:

$$\ln\left(\frac{I(\lambda)}{E(\lambda)}\right) = \sum_p c_p \lambda^p - \sum_j N_{s,j} \sigma_j(\lambda) \qquad \text{8-1,}$$

Here, $I(\lambda)$ is the radiance measured at the instrument, $E(\lambda)$ is the extra-terrestrial irradiance without absorption, λ is the wavelength, σ_j is the absorption cross-section of absorber j, $N_{s,j}$ is the slant column density of absorber j, and c_p are the coefficients of a polynomial in wavelength representing broad band extinction by scattering. The slant column density of absorber j is defined as its concentration n_j, integrated along the light path

$$N_{s,j} = \int n_j(s)\, ds \qquad \text{8-2,}$$

In a real measurement, radiances are measured for discrete wavelength intervals, and the DOAS equation is written in a discrete form:

$$\ln\left(\frac{I(\lambda_i)}{E(\lambda_i)}\right) = \sum_{p=0}^{P} c_p \lambda_i^p - \sum_j N_{s,j} \sigma_j(\lambda_i) + \varepsilon(\lambda_i) \qquad \text{8-3,}$$

Here, $\epsilon(\lambda_i)$ is the residual at wavelength λ_i, which accounts for measurement noise and all effects not captured by the simple model used.

If all measurements in a spectral region (the fit window) are treated simultaneously, equation 8-3 represents a system of linear equations with the unknowns $N_{s,j}$ and c_p which can be solved by a linear least squares fit minimizing $\sum \epsilon(\lambda_i)^2$.

A number of additional effects need to be considered in a DOAS retrieval:

8.2.1.1 Convolution with the instrument spectral response function (ISRF)

In a real measurement, the signal from an individual detector pixel does not represent a monochromatic radiance, but the integral over the wavelength range covered by the pixel. In addition, the optical system of the spectrometer results in a smoothing of the radiances reaching the detector. The combination of the two effects is described by the ISRF, and the measured radiance (and irradiance) can be written as the convolution of the monochromatic quantities with the ISRF:

$$I(\lambda_i) = \int S(\lambda; \lambda_i)\, I(\lambda) d\lambda \qquad \text{8-4.}$$

In the DOAS analysis, this is accounted for by simply convoluting high resolution absorption cross-sections σ(λ) with the ISRF. This is mathematically not correct, but for small absorptions, it can be shown to be a good approximation. In case of the chlorine dioxide retrieval, all trace gas absorptions can be considered to be small and no additional corrections such as the so called I_0 correction (Aliwell et al., 2002) are applied to the absorber cross-sections.

8.2.1.2 Temperature dependence of the absorption cross-sections

In equation 8-3, a possible temperature dependence of the absorption cross-sections is not accounted for. However, many absorption cross-sections have temperature dependencies, and as result of atmospheric variations of temperature in time, space and altitude, the radiance observed at the satellite is the effect of absorptions by molecules at different temperatures. In the case of the chlorine dioxide retrieval, this is in particular the case for O_3. In first approximation, the temperature dependence of the O_3 cross-section can be described as a linear combination of absorption cross-sections taken at two different temperatures, and this approach is used for the chlorine dioxide retrieval by including two O_3 cross-sections in the DOAS fit.

The temperature dependence of the chlorine dioxide absorption itself is not well known and therefore no correction is included for this.

8.2.1.3 Change of light path over the fitting window

One of the basic assumptions in the separation of spectral retrieval and radiative transfer applied in the DOAS method is that there is a representative light path length for the entire spectral range used in the DOAS fit. In the real atmosphere, this is usually not the case as the light path length depends on many parameters such as the scattering probability, the surface reflectance and the optical depth of the atmosphere, which all depend on wavelength. Nevertheless, the assumption of a constant light path can be made if

- the fitting window is small enough to represent the wavelength dependency of Rayleigh scattering by a linear increase,
- the absorption of trace gases in the fitting window is small, and
- there are no large spectral changes in surface reflectance.

For the chlorine dioxide retrieval, these criteria are fulfilled, and no additional corrections for the wavelength dependency of the air mass factor such as described in Puķīte et al. (2016) are included.

8.2.1.4   Effect of inelastic scattering

Inelastic scattering is not considered explicitly in the DOAS equation, which is monochromatic and does not allow for redistribution of photons to different wavelengths. The main effect of rotational Raman scattering in the atmosphere can be modelled by introducing a pseudo-absorber, a so-called Ring cross-section (Solomon et al., 1987), calculated with a radiative transfer model, and included in the fit (see Section 8.2.2.2). This accounts for the spectral signature of the filling-in of Fraunhofer lines by rotational Raman scattering but not of atmospheric absorption structures (Fish and Jones, 1995). Inelastic scattering in liquid water can be relevant over oceans and in principle can be treated in the same way. However, vibrational Raman scattering is ignored here as it can in good approximation be approximated by the additive offset correction (Vountas et al., 2003).

8.2.2   Implementation in the DOAS module

In the DOAS module, solving the DOAS equation is implemented as part of a more convolved scheme, because additional steps have to be taken which are related to spectral calibration, spectral interpolation and treatment of outliers for the radiance and irradiance spectra. This is described in the following sections. A detailed flow diagram of the DOAS module is given in Figure 8.2.
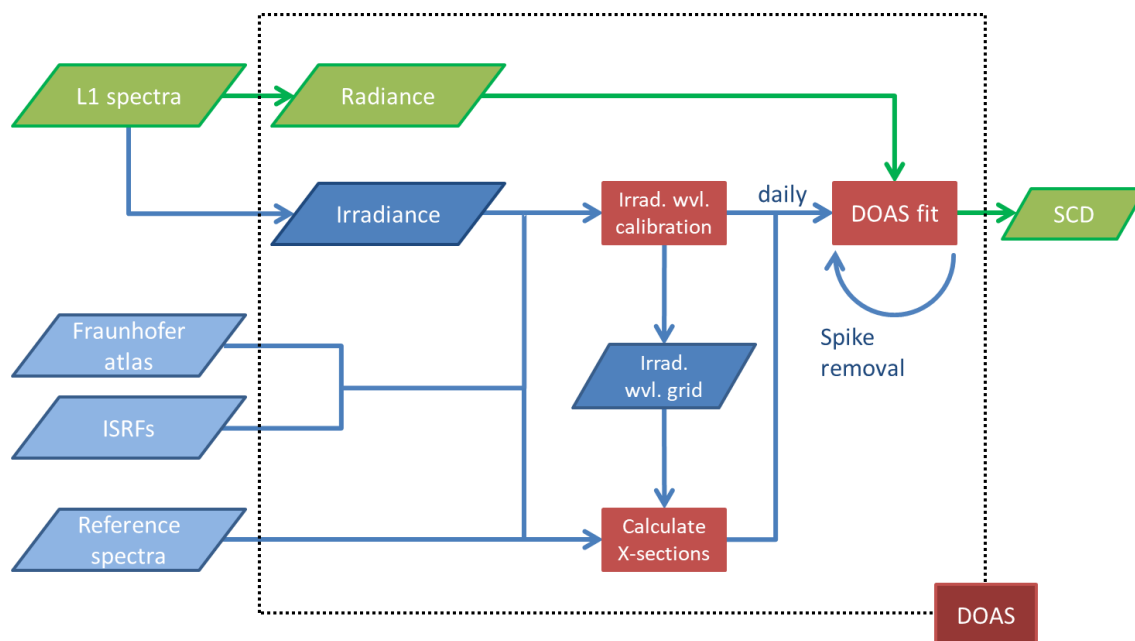
Figure 8.2: The structure of the DOAS algorithm module.

The chlorine dioxide fit window extends from 345 to 389 nm. A large fit window is preferred as more spectral points make for a smaller noise error. The degree of the polynomial is 5 (i.e. 6 coefficients), which sufficiently captures the spectral variation of atmospheric scattering and surface reflection across the fit window.

The DOAS module outputs slant column densities with an estimate of their uncertainties. The error in the spectrum (considered as a white noise error) is estimated from the root-mean-square deviation of the fit and subsequently propagated to an error in the retrieved slant column. Here, the root-mean-square deviation Δ_{RMS} is defined according to

$$\Delta_{RMS}^2 = \frac{1}{m} \sum_{i=1}^{m} \left[y_{meas}(\lambda_i) - y_{fit}(\lambda_i) \right]^2 \qquad \text{8-5,}$$

where y is the logarithm of the sun-normalized radiance, and m is the number of spectral points used in the final fit. The error covariance matrix **S** for the vector of fit parameters is given by

$$\mathbf{S} = \frac{m}{m-n} \Delta_{RMS}^2 \left(\mathbf{\kappa}^T \mathbf{\kappa} \right)^{-1} \qquad \text{8-6,}$$

where n is the number of fit parameters, m-n is the number of degrees of freedom of the estimator and **K** is the matrix of coefficients of the linear model (λ_i^p and $\sigma_j(\lambda_i)$). The error in the chlorine dioxide slant column is the square root of the corresponding diagonal element of **S**.

8.2.2.1   Selection of background spectrum

For the S5p chlorine dioxide retrieval, daily irradiance spectra as measured by S5p are used as background spectra.

8.2.2.2   Reference spectra and absorption cross-sections

In addition to the target species chlorine dioxide, other trace gases that show significant absorption in the fit window are O_3 (at two temperatures), NO_2, O_4 and BrO. These absorbers are complemented by several pseudo-absorbers, which are included to compensate other spectral effects. These special cross-sections include

- a Ring cross-section to account for rotational Raman scattering in the atmosphere
- two cross-sections to account for an additive radiation offset which changes linearly with wavelength
- two cross-sections to account for the effect of changes in the wavelength registration (Beirle et al., 2013)
- two cross-sections compensating the effect of inhomogeneous scenes
- two cross-sections needed to reduce systematic biases in the OClO columns

A list of all absorbers and their reference spectra is given in Table 8.2. Figure 8.3 shows the cross-sections of all molecular absorbers. Discussion on how the absorption cross-sections $\sigma(\lambda_i)$ for the different absorbers are calculated is given below.

Table 8.2: Absorbers and pseudo-absorbers included in the DOAS and the source of their reference spectra.

Absorber	Reference spectrum	Remark
Chlorine dioxide	(Kromminga et al., 2003)	Fixed reference temperature of 213 K.
NO₂	(Vandaele et al., 1998)	Fixed reference temperatures of 220 K.
O₃	(Serdyuchenko et al., 2014)	Reference temperatures of 223 K and 243 K.
O₄	(Thalman and Volkamer, 2013)	Fixed reference temperature of 293 K.
BrO	(Wilmouth et al., 1999)	Fixed reference temperature of 228 K, fixed column from second fit.
Ring	$\ln\left(\dfrac{\int S(\lambda_i, \lambda) I_{Ray+Ram}(\lambda) d\lambda}{\int S(\lambda_i, \lambda) I_{Ray}(\lambda) d\lambda}\right)$	Calculated with SCIATRAN according to Vountas (1998).
Radiance offset	$1/E_0(\lambda_i)$ and $(\lambda - \lambda_c)/E_0(\lambda_i)$	May also capture Ring deficiencies and vibrational Raman scattering effects
Empirical cross-sections derived from mean residual	Special DOAS fit excluding OClO See section 8.2.2.3	Will capture systematic residual structures from instrumental effects and atmospheric absorption not yet described by absorbers listed above

The absorption cross-sections for the trace gas retrieval are determined from high-resolution reference spectra according to Equation 8-4 by convolving them with the nominal S5p ISRF. This is done for each row independently. In many DOAS implementations, a polynomial of degree P is fitted to the reference spectrum and the resulting polynomial is subsequently subtracted, but this is not necessary and only affects the values of coefficients of the closure polynomial $c_p(\lambda_i)$. All absorption cross-sections are prepared in this way on a high-sampling wavelength grid of 0.01 nm for all row dependent ISRFs offline. In the DOAS module, the absorption cross-sections are then interpolated to the actual irradiance wavelength grid (cubic spline interpolation).

The Ring spectrum is calculated from two SCIATRAN radiance simulations at high spectral resolution, one including the effect of inelastic Raman scattering and the other one excluding it. These spectra are calculated for a Rayleigh only atmosphere in a typical scenario and thus do not include the variability of the Ring effect with surface albedo, observation geometry or clouds. They also do not include the effect of filling in of chlorine dioxide absorption structures. The Ring pseudo cross-section is then calculated from the ratio of the two spectra, each convoluted with the instrument slit function:

$$\sigma_{Ring}(\lambda_i) = \ln\left(\frac{\int S(\lambda_i, \lambda) I_{Ray+Ram}(\lambda) d\lambda}{\int S(\lambda_i, \lambda) I_{Ray}(\lambda) d\lambda}\right) \qquad \text{8-7.}$$

Again, this is done for each row dependent ISRF offline, and only interpolation to the wavelength grid of the actual irradiance is performed in the DOAS module.
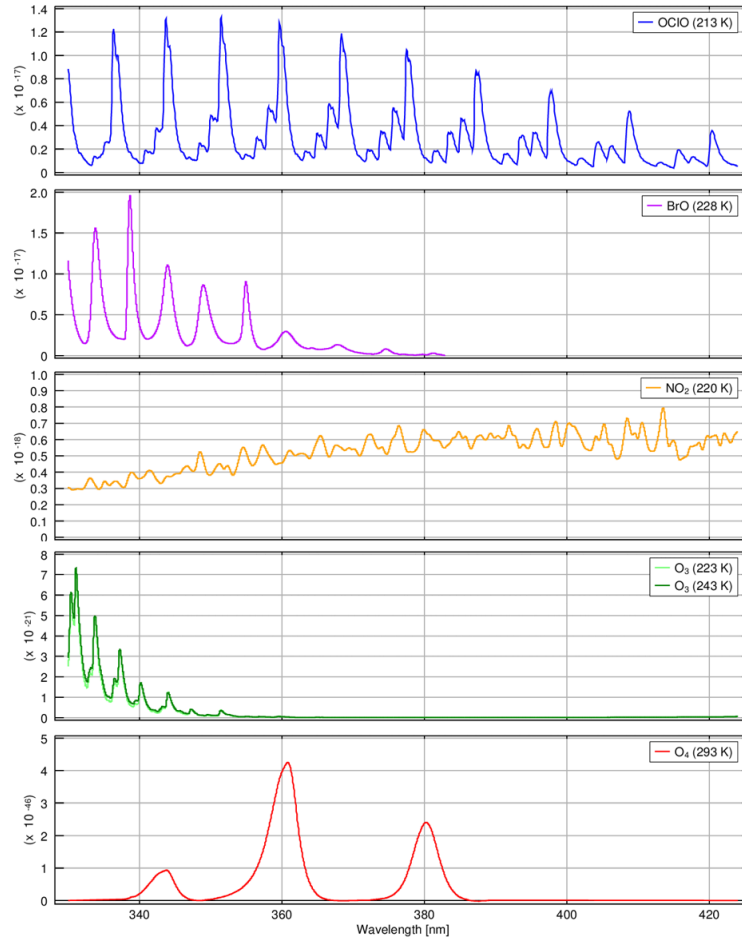
Figure 8.3: Absorption cross-sections of fitted trace gases in units of cm^5 molec^{-2} for the oxygen dimer (O$_4$), and cm^2 molec^{-1} for all other trace gases.

Residual instrument stray light (i.e. stray light that is not corrected in the Level-1b processor), vibrational Raman scattering and fluorescence can result in an additive radiance offset. For small additive offsets $A(\lambda_i)$ to the measured radiance, a pseudo-absorber can be added to the summation in Equation 8-3, whose cross-section is given by the offset's differential part according to

$$\sigma_{add}(\lambda_i) = \left(\frac{A(\lambda_i)}{I(\lambda_i)} \right)$$

8-8,

where $I(\lambda_i)$ is the measured radiance. This makes solving the DOAS equation somewhat impractical to implement because the offset cross-section needs to be determined again for every pixel. Moreover, in the case of larger absorptions, the offset cross-section and other absorption cross-sections may become linearly dependent. Instead, the offset cross-section is assumed to be inversely proportional to the solar irradiance $E(\lambda)$, which has proven to give good results. For the OClO retrieval, the offset is assumed linear in wavelength, and two cross-sections are included, one for the offset, the other for the slope:

$$\sigma_{offset}(\lambda_i) = \left(\frac{1}{E(\lambda_i)}\right)$$
<div align="right">8-9.</div>

$$\sigma_{slope}(\lambda_i) = \left(\frac{\lambda - \lambda_c}{E(\lambda_i)}\right)$$
<div align="right">8-10.</div>

Here, λ_c is the centre wavelength of the fitting window. As the solar irradiance wavelength grid is used throughout the DOAS module, the offset cross-section does not need to be interpolated in wavelength. It also does not need to be convoluted with the S5p ISRF.

8.2.2.3 Empirical cross-sections for bias correction

The spectral retrieval of chlorine dioxide, using only absorption cross-sections from the literature, suffers from negative biases that show a latitudinal and / or regional as well as a seasonal dependence. Often, such biases are corrected using a reference sector, cf. Section 8.3, or measurements at low Sun are filtered out. However, as chlorine dioxide can be present in the entire Polar region at twilight, there is no "clean region" and a correction for latitudinal biases cannot easily be computed.

A different approach is to correct the negative biases by the inclusion of empirical absorption cross-sections that are computed by averaging residuals of a specialized DOAS fit. This specialized fit uses the same settings as the standard-fit but excludes the cross-section of chlorine dioxide. The mean residual of chlorine dioxide free scenes can then be regarded as a summary of all spectral features not yet accounted for. Including the mean residual in a second fit can then be used to compensate the deficiencies in the usual DOAS fit. Such deficiencies may originate from instrumental effects e.g. differences between the solar irradiance and the backscattered radiance spectra, but also from unknown absorbers along the light path. Such a mean residual usually only needs to be computed once and can be applied to the whole time series.

The effectiveness of this correction depends strongly on the spatio-temporal selection criteria for the averaging of residuals. For the chlorine dioxide fit, it is assumed that unaccounted spectral structures lead to systematic biases. The region and time for the averaging of residuals is then selected by:

a) Computing a time series of chlorine dioxide slant column densities
b) Identifying regions and times with the largest biases
c) Excluding periods / regions (determined in b)) where chlorine dioxide may be present
d) Running the special DOAS fit without the chlorine dioxide cross-section for the region in c) and saving the residual of each fit
e) Averaging the residuals from step d) for each of the 450 rows individually

The residual of a single measurement $\epsilon(\lambda_i)$ can be computed by rearranging Equation 8-3. The empirical row dependent pseudo-cross-section σ_{res} can then be computed from

$$\sigma_{res}(\lambda_i, y) = \frac{1}{M_y}\sum_m^{M_y} \epsilon_m(\lambda_i, y)$$
<div align="right">8-11.</div>

Where λ_i is an individual wavelength, y denotes the detector row, m is a measurement in the selected region and M_y is the total number of measurements in the region.

For the current version of the processor, two regions with strong negative biases were identified and the corresponding mean residuals of these regions were included as separate pseudo absorbers. These pseudo absorbers are only calculated once and are then applied to the whole time series. In the processing, these are treated as static inputs, just like any other trace gas cross-section. These mean residuals were derived from single orbits as listen in Table 8.3.

Table 8.3: Input files and selection criteria for the calculation empirical cross-sections

Radiance file	Latitude bounds	Longitude bounds
S5P_OFFL_L1B_RA_BD3_20190201T 185314_20190201T203444_06759_ 01_010000_20190201T221649.nc	-30, -10	200, 270
S5P_OFFL_L1B_RA_BD3_20190622T 081057_20190622T095227_08753_ 01_010000_20190622T114235.nc	60, 90	0, 360

Figure 8.4 shows the derived mean residuals as a function of wavelength. Here the mean residuals are shown for row 225; differences to other rows are small but relevant.
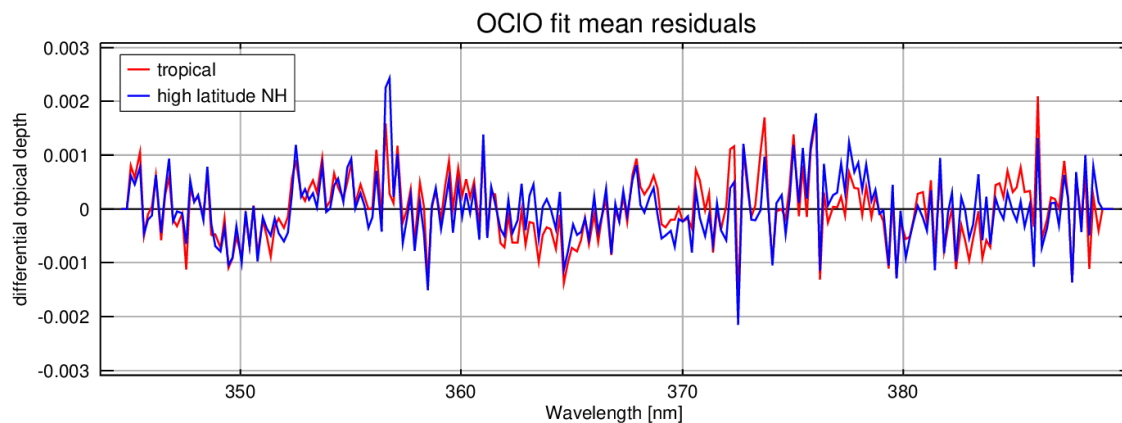
Figure 8.4: Mean residual derived from a specialized DOAS fit in two different regions and seasons for row 225, cf. Table 8.3.

The geographical distribution of the retrieved monthly mean fit coefficients is shown in Figure 8.5 for an arbitrary month (February 2020). Looking at the maps, the spatial pattern is quite similar, but the values are anti-correlated.

2020-02

Fit coeff [NH high Latitudes]

Data Min = -4,202, Max = 2,797, Mean = -0,6144

2020-02

Fit coeff [eq. Pacific]

Data Min = -5,019, Max = 3,006, Mean = -0,3516
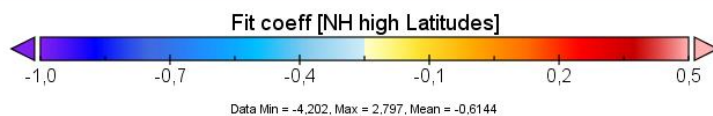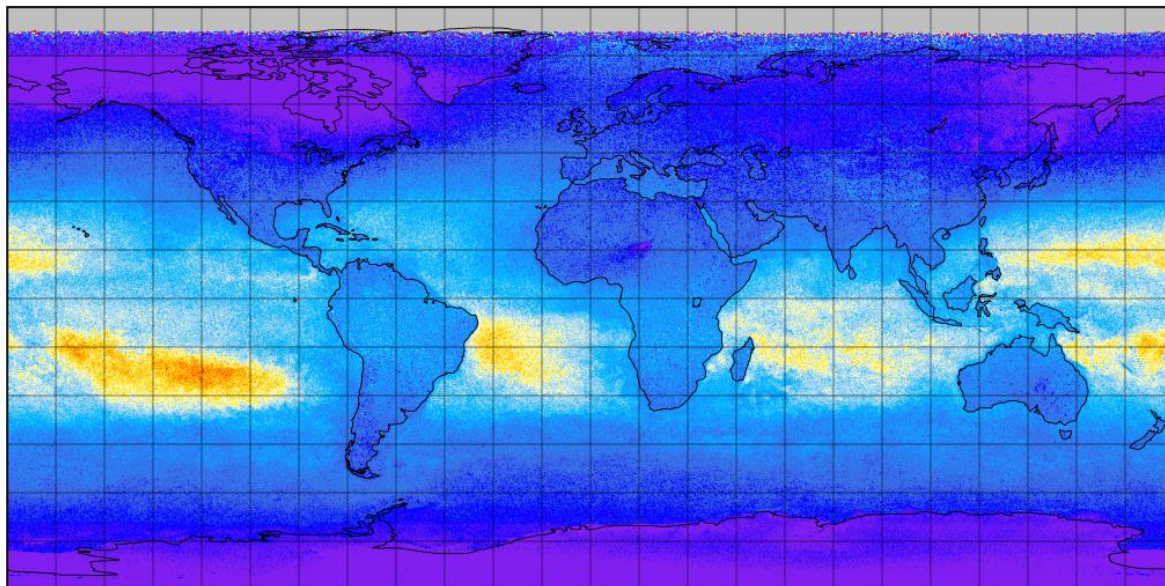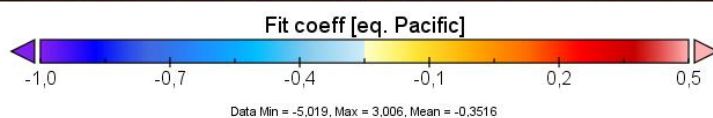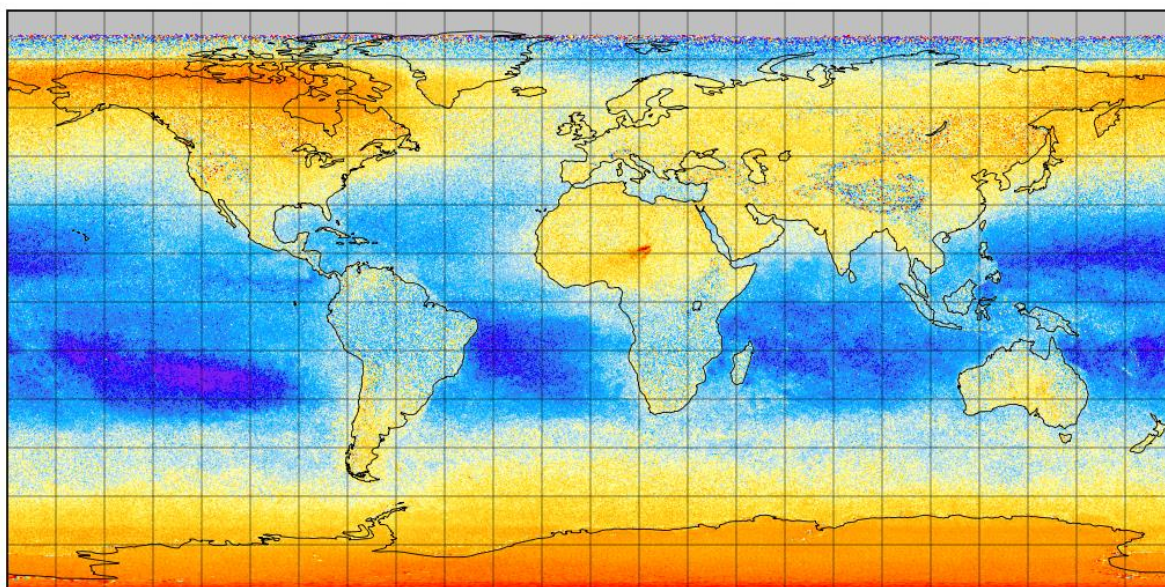
Figure 8.5: Monthly means of fit coefficients of the two empirical cross-sections.

8.2.2.4 Empirical cross-sections for scene inhomogeneity correction

It has been shown, that for many products of push-broom imaging spectrometers, inhomogeneous scenes (scenes containing large gradients in intensity) can lead to large residuals and biases (Richter et al., 2018). This is mainly because of the change in wavelength registration and slit function associated to such measurements. While the wavelength shift is efficiently corrected by the linearized shift and stretch parameters (see section 8.2.2.7), strongly increased residuals and artefacts in the OClO slant columns remain for inhomogeneous scenes. Regions where such artefacts can be observed in the data are the sea ice edge, the margins of snow-covered areas including Iceland and Greenland, and cloud edges over dark surfaces.
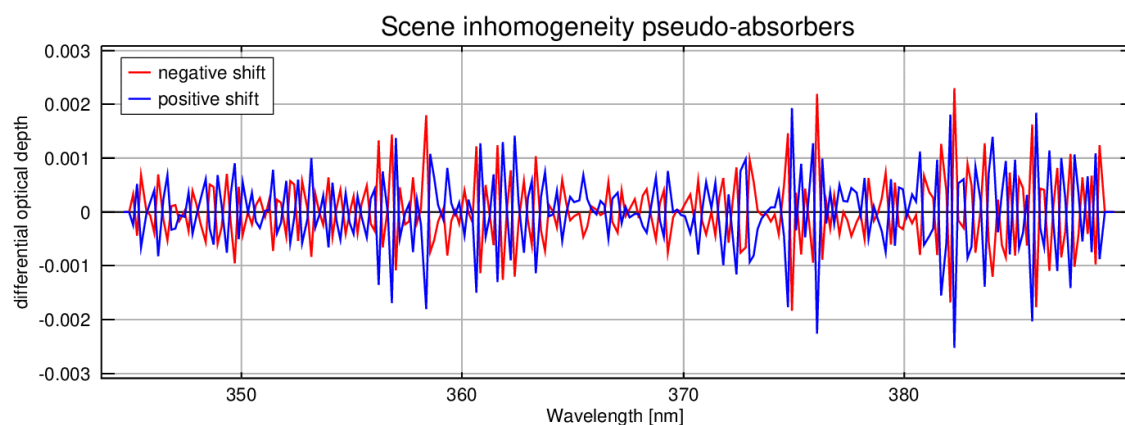
Figure 8.6: Pseudo absorbers correcting for the effects of scene inhomogeneity

The effect can largely be reduced by including two additional cross-sections in a similar approach as discussed in section 8.2.2.3. They are computed in the following way:

1. A standard OClO retrieval is performed including all cross-sections.
2. A second retrieval is performed, where no OClO is included. The residuals of this fit are saved
3. From the residuals, two groups are selected and averaged – those having a large negative spectral shift and those having a large positive spectral shift. The averaging is performed by row, resulting in a total of 900 cross-sections.

The resulting cross-sections for row 225 are shown in Figure 8.6. They are nearly mirror images of each other but some small differences exist, leading to better fit results when including both of them in the retrieval.

8.2.2.5 Treatment of BrO absorption

BrO has some absorption bands in the OClO fitting window, and therefore needs to be included in the fit in order to avoid biases in situations of large BrO absorption for example in Polar spring. Unfortunately, simply including the BrO cross-section in the fit does not lead to robust fitting results. Therefore, the approach of Puķīte et al., 2021 is followed, who suggested to include BrO as a non-fitted parameter in the retrieval using the BrO slant columns retrieved in a second fit tailored for BrO

retrievals. For the BrO columns, the retrieval of Seo et al., 2019 is used in a version using the daily S5p irradiance as background.

8.2.2.6 Treatment of outliers

Particularly in the region of the South Atlantic Anomaly, outliers occur for individual detector pixels that may reduce the fit quality. For polar orbiting satellites, an outlier-removal scheme is therefore implemented when solving the DOAS equation. A detailed description can be found in Richter et al, (2011). A brief summary of the procedure is as follows: In the outlier-removal scheme, after the linear DOAS equation is solved for the first time, an analysis of the residual is performed to identify outliers. Spectral points are labelled as outliers if the difference between measured and fitted spectrum (i.e. the logarithm of the sun-normalized radiance) is larger than a threshold value times the root-mean-square error of the fit (Equation 8-5) excluding all outliers identified so far. The spectrum is searched repeatedly until all outliers have been removed or a maximum number of spectral outliers has been reached. If outliers are identified, they are removed from the spectrum and the DOAS equation is solved a second time and the outcome of this calculation is the final reported retrieval solution. In the current version of the OClO product, this outlier removal is not applied.

8.2.2.7 Spectral calibration

As the solar spectrum is highly structured by Fraunhofer lines and the absorption of chlorine dioxide is weak in comparison, even small differences in the wavelength registration of I and E can lead to large residuals. In addition, small spectral misalignment between the reflectance and the absorption cross-sections can cause significant biases in the retrieved slant columns for the absorbers.

Although a general wavelength calibration is performed in the Level-1b processor, additional spectral calibration steps are taken in the chlorine dioxide Level-2 algorithm to further improve the accuracy of retrieved slant columns. More specifically, the radiance and irradiance need to be absolutely wavelength calibrated and brought onto the same grid.

The Level-1b product provides radiance and irradiance spectra on a nominal wavelength grid $\lambda_{i,nom}$ that is supposedly different from the true wavelength grid nodes $\lambda_{i,true}$. The offset between the two wavelength grids may in turn depend on wavelength. Here only linear variations are considered and a constant wavelength shift (s_0) and a stretch / squeeze parameter (s_1) are fitted as discussed below.

As the first step, the irradiance measured daily for every detector row is wavelength calibrated by using a high-sampling solar irradiance reference spectrum. This reference spectrum $E^{ref}(\lambda_{true})$ is calculated from a high-resolution irradiance spectrum or Fraunhofer atlas (Chance and Kurucz, 2010) by convolution with the S5p ISRF. If the true wavelengths are written as $\lambda_{true} = \lambda_{nom} + s_0 + s_1 \cdot (\lambda_{nom} - \lambda_c)$, where λ_c is some (arbitrary) reference wavelength at for example the centre of the fit window, the following equation is solved

$$\ln\left(E_{meas}(\lambda_{i,nom})\right) = \ln\left(E^{ref}\left(\lambda_{i,nom} + s_0 + s_1 \cdot (\lambda_{i,nom} - \lambda_c)\right)\right) \\ + \sum_p c_p \lambda_{i,nom}^p + \varepsilon(\lambda_i)$$

<div align="right">8-12.</div>

The polynomial of, for example, degree four or five accounts for variation of the sun-earth distance, and radiometric calibration and degradation offsets. As the equation is non-linear, its least-squares solution for the shift and stretch parameters (s_0 and s_1) and the polynomial coefficients is found iteratively (Levenberg-Marquardt scheme). Since the reference spectrum $E^{ref}(\lambda_{true})$ is available at a high sampling of 0.001 nm, interpolation errors will be small (cubic spline interpolation is used). Derivatives needed to calculate the update during iteration are approximated by difference quotients. Once the fit has converged, the true wavelength grid node values of the measured irradiance $\lambda_{i,true}$ can be calculated. This is the wavelength grid on which the cross-sections are prepared, and the DOAS fit is performed.

A similar non-linear wavelength calibration is needed for the radiances, only that they are not aligned to the external Fraunhofer atlas but to the current wavelength corrected S5p irradiance measurement. As the radiances include atmospheric extinction, Equation 8-12 needs to be extended by the slant columns term:

$$\ln\left(I\left(\lambda_{i,nom} + s_0 + s_1 \cdot (\lambda_{i,nom} - \lambda_c)\right)\right) = \ln\left(E(\lambda_i)\right) - \sum_j N_{s,j}\sigma_j(\lambda_i) \\ + \sum_p c_p \lambda_i^p + \varepsilon(\lambda_i)$$

<div align="right">8-13.</div>

In the current algorithm, this is achieved by performing a linear DOAS retrieval and including the shift and squeeze parameters in the linearized form as proposed in (Beirle et al., 2013).

All equations, including the DOAS equation, are solved using non-weighted least squares (i.e. the covariance matrix of the measurement is the identity matrix) and the uncertainties in the Level-1b product are not used. Finally, it should be noted that the spectral calibration steps described here are expected to also largely account for effects of partial illumination of the instrument slit.

8.3 Offset correction and de-striping of slant columns (POST)

Before slant columns are further processed, an offset correction may be applied in the post-processing module POST. Small errors in sun-normalized radiance spectra that vary quasi-randomly between the different rows of the CCD but are relatively constant in time can result in systematic column density offsets that show up in maps as a characteristic striping pattern overlaid on top of the geophysical variation of chlorine dioxide columns. Striping effects are characteristic for imaging spectrometers that use a two dimensional detector instead of a linear detector with across-track scanning (for the latter, the same effect can lead to constant offsets, which are more difficult to detect). For polar-orbiting satellites such as OMI and TROPOMI, stripes run in the meridional direction. Although striping offsets in the current version of the algorithm are about one order of magnitude smaller than the precision of the observations, destriping is performed in the retrieval.

In addition to stripes in OMI and TROPOMI data, latitude and region dependent biases are observed in all chlorine dioxide slant column products of all sensors. The reasons are not fully understood, but are likely related to differences between solar irradiance spectra and backscattered radiance. In addition, spectral interference between chlorine dioxide and spectral structures of surface reflectance plays a role both over land and clear water ocean regions. There also appears to be spectral cross-talk between Ring corrections and chlorine dioxide. As the offsets can be as large as typical chlorine dioxide slant columns in Polar Regions, correction schemes have been applied for the GOME, SCIAMACHY and GOME-2 OClO products.

The S5p OClO product is characterized by very small offsets compared to products from other sensors. Nevertheless, as part of the destriping procedure, an implicit offset correction is applied.
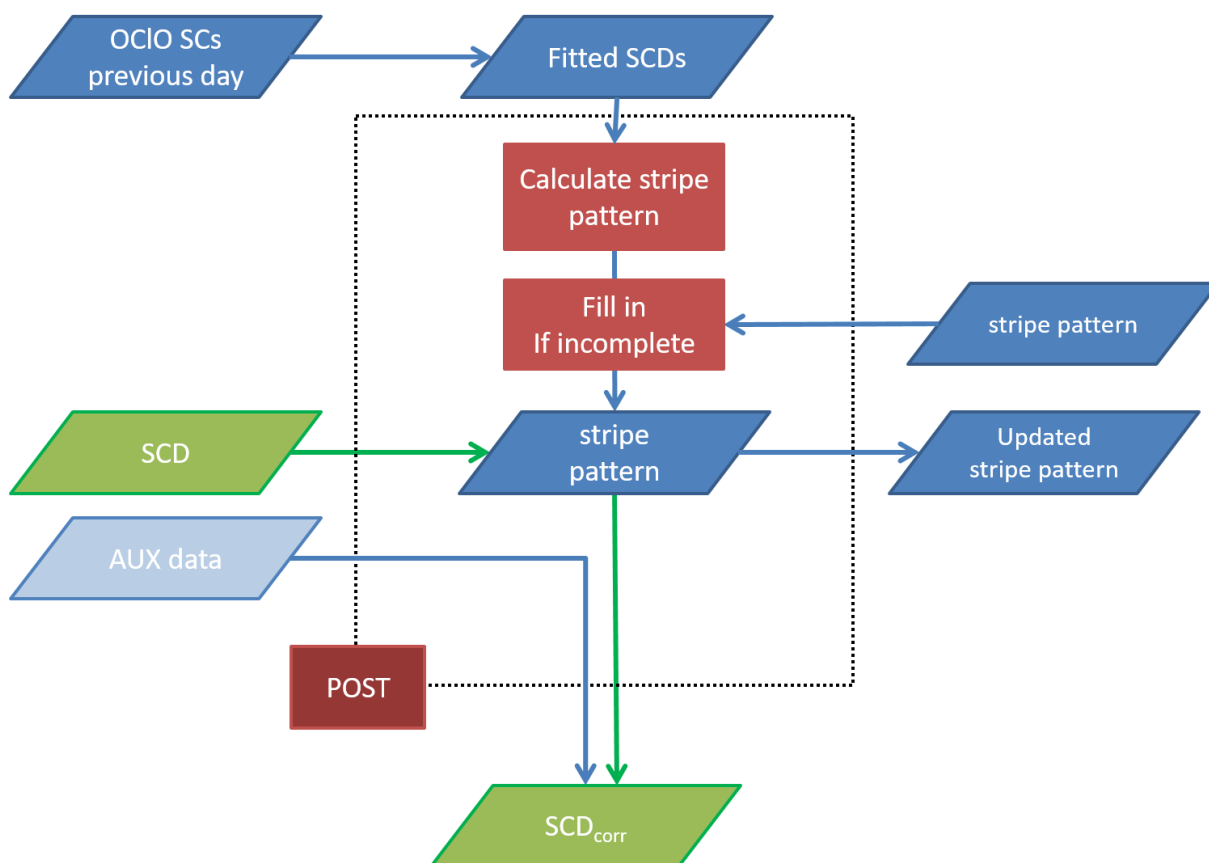
Figure 8.7: The structure of the POST algorithm module

A detailed flow diagram of the POST module is given in Figure 8.7. Additive offsets to fitted slant columns are assumed that may depend on latitude but this dependence is not included. Such a correction scheme is only possible if a clean region (absence of OClO) is available. In addition, a high frequency contribution of the offset depending on the across-track pixel index (striping) is assumed. Both terms are determined from fitted slant columns over pixels for which low chlorine dioxide columns are expected. As a starting point, the Pacific region (30°S-30°N, 160°W-220°W) is used.

Slant columns from the current day are used to compute both the offset and the striping pattern. In case data is missing, the last valid values are used from previous days. In an operational environment, offset correction can also be based on measurements from the previous day with little impact on uncertainties. This enables data delivery in near real time as there is no need to first assemble a full day of data.

Denoting the across-track pixel index by y, which assumes 450 discrete values, and assuming that latitude is the relevant variable, the fitted slant columns can be written as

$$N_s^{fit}(t, y) = N_s(t, y) + c(t) + A(y) \qquad \text{8-14,}$$

where $c(t)$ is the offset of the de-striped slant columns and $A(y)$, is the striping offset. If the OClO slant column can be assumed to be 0, the sum $A^*(y) = c(t) + A(y)$ can be directly determined from the row dependent means in the reference region:

$$A^*(y) = \frac{1}{M_y} \sum_m^{M_y} N_s^{fit}(m, y) \qquad \text{8-15,}$$

Here, m denotes an individual measurement in the reference region and M_y is the total number of measurements for row y in the region. Basic quality filtering is applied for m and M_y to exclude measurements having a bad fit quality. The filters applied are

- SZA <= 50°
- Mean radiance <= 8x10^{13}
- $\chi^2 \leq 0.01$

The striping pattern $A^*(y)$ can then be subtracted from all slant columns by row y.

For practical reasons, the POST processor also includes additional external data in the OClO l2 files. In the current product, these additional data are

- Cloud fraction and cloud pressure from the OFFL NO$_2$ product
- ECMWF Potential Vorticity at 50 mbar, linearly interpolated to the time and position of the measurement.

8.4 Calculation of air mass factors

For OClO products from previous missions, no vertical column densities were provided. Instead, the slant column density was the final product (Valks et al., 2017). Nevertheless, it appears possible to derive a VCD of chlorine dioxide that not only corrects for the length of the light path through the absorbing layer, but also corrects for loss of chlorine dioxide by photolysis in twilight. To do so, the air mass factors have to account for the variation of OClO concentration as a function of local SZA. A similar problem exists for NO$_2$, and can be solved by applying chemically modified AMFs (Roscoe et al., 2001).

In the current S5p OClO product, no conversion to vertical columns is performed. This may be added in a future version of this product.

9 Feasibility

9.1 Computational effort

The computational effort of the OClO product is low as it is a standard product and currently does not include an AMF calculation:

- DOAS fitting of one orbit of S5p data (1.6 million pixels) takes 250 seconds on one core of a standard Intel i7 CPU. Radiances and irradiances were already available locally for this test so file transfer times will have to be added.
- Post processing takes about 120 seconds per orbit on the same processor.
- The size of the output files is currently 200 Mbyte / orbit, but this may increase in future versions if vertical columns and averaging kernels are to be included in the output.

In summary, the computational load of this product is low and the output file size similar to other S5p lv2 products.

9.2 Input data

The required input data can be separated into static and dynamic inputs. Static inputs, such as the absorption cross-section of absorbers, do not change with time and only need to be stored once. Dynamic inputs, such as the radiance and irradiance spectra change over time.

9.2.1 Static input

Static input data for the OClO retrieval have been briefly discussed in section 8 and include cross-sections and solar Fraunhofer atlas. They are available from the literature, cf. Table 8.2. In addition, the ISRF is required which is available from the S5p project.

9.2.2 Dynamic input

The main input data for the S5p OClO product are TROPOMI level 1 products of band 3 radiance and irradiance. As discussed in section 5, global coverage can be achieved with little effort and thus global data is required. If data volume is a problem, the regions of interest can be limited to latitudes > 40° but this is not foreseen at this point.

In addition to the TROPOMI lv1 data, TROPOMI NO2 OFFL data are used to extract cloud information which is added to the OClO lv2 files. Potential Vorticity at 50mbat is also included from ECMWF forecast data.

9.3 Output Product Overview

The current output format of the L2 OClO files produced by this scientific algorithm follows closely the current conventions of the operational products, in terms of filename and content structure as well as variable name nomenclature. The output files are in NetCDF-4, with the convention CF.

A typical L2 OClO filename is structured as:

S5P_IUPB_L2__OCLO___20220401T010743_20220401T024913_23135_02_009700_20230207T161154.nc

where the two first time stamps in yellow correspond to start and end of the orbit, the orbit number is in green, the grey substring is inherited from the collection of the L1 data, the red part is the product version number (v00.97.00 in this example) and the creation date and time are in cyan.

The data fields contained in the output of the breadboard algorithm including all variables and coordinates and attributes is displayed in Table 13.1 in appendix A.

10 Error analysis

Uncertainties in the chlorine dioxide product are inherent to all steps in the retrieval, namely the spectral retrieval, offset correction and the possible application of the air mass factor. In the following, the sources of uncertainties in the individual retrieval steps are discussed.

10.1 Uncertainties on slant columns

Uncertainties in the slant columns are related to noise of the spectra, errors of the laboratory cross-sections used, imperfect knowledge of the actual slit function, instrumental effects, and spectral interference with other absorbers in the fit window. All sources of uncertainty are subject to random as well as systematic errors that often cannot be separated. It can be assumed, that the noise on the spectra is generally randomly distributed for a constant intensity. However, with decreasing intensity, the relative contribution of shot noise to the measured signal increases. As chlorine dioxide can only be measured in twilight, the fit quality is generally worse than for measurements at small solar zenith angles (and large intensities). Over the course of the lifetime of S5p, degradation may affect the measured spectra and potentially lead to temporal drifts. Furthermore, the spectral retrieval may be impacted by differences between the solar irradiance and the backscattered radiance spectrum, which may lead to spectral structures.

The laboratory cross-sections affect the spectral retrieval in two ways – the error in the measured cross-section itself and the temperature dependence of the cross-section. For the chlorine dioxide cross-section used, the reported statistical error is smaller than 5% (Kromminga et al., 2003). The impact of the temperature dependence is expected to be negligible, because chlorine dioxide is found only in the stratosphere and atmospheric temperatures are expected to be close to the assumed temperature of 213 K.

The slit function (or ISRF) is used to convolve the cross-sections. When the actual slit function of the measurements differs from the slit function determined in the laboratory, high-frequency residual structures are created in the DOAS retrieval that may interfere with the absorbers of interest. Varying slit functions can be caused by thermal instabilities of the spectrometer, but can also be caused by the inhomogeneous illumination of the entrance slit, which also causes a wavelength shift (Noël et al., 2012). The effect of changes of the slit functions on the retrieval can, in principle, be corrected by the inclusion of an empirical pseudo-absorber cross-section. As chlorine dioxide is found mainly in polar regions, the edges between ice and land surface / ocean are regions where inhomogeneous illumination occurs. These problems are largely compensated by the pseudo absorbers included in the fit.

Spectral cross-talk between the chlorine dioxide and other absorption and scattering signatures in the optical depth may lead to biases. The latter can be large and lead to unphysical negative or large chlorine dioxide columns in particular at high latitudes, but also elsewhere. As chlorine dioxide is only found at high latitudes and large solar zenith angles, the impact on the product is rather large. So far, no settings in the spectral retrieval could be found to fully suppress such time and latitude dependent biases based on known atmospheric effects. However, the magnitude of the negative bias is strongly reduced by the inclusion of empirical pseudo-absorber cross-sections calculated from the mean residual (see section 8.2.2.3). An offset correction is applied to further reduce the effect on the slant columns, as discussed in more detail in section 7.2.3. However, the impact of this correction is small.

The bias and precision of the retrieved chlorine dioxide slant column density may be estimated from the distribution in a clean region. Figure 10.1 shows a histogram of the retrieved slant columns in the equatorial Pacific for a single day, where no chlorine dioxide is expected. The mean of the distribution can be regarded as the bias, while the standard deviation is a measure for the precision. The distribution shows a very small bias of 8.5×10^{11} molec / cm^2, which is about two orders of magnitude smaller, than the chlorine dioxide values found in the polar vortex during chlorine activation periods. The precision determined is about 1.97×10^{13} molec / cm^2, but is expected to be poorer in twilight conditions, due to the larger contribution of shot noise to the measured radiance spectra.
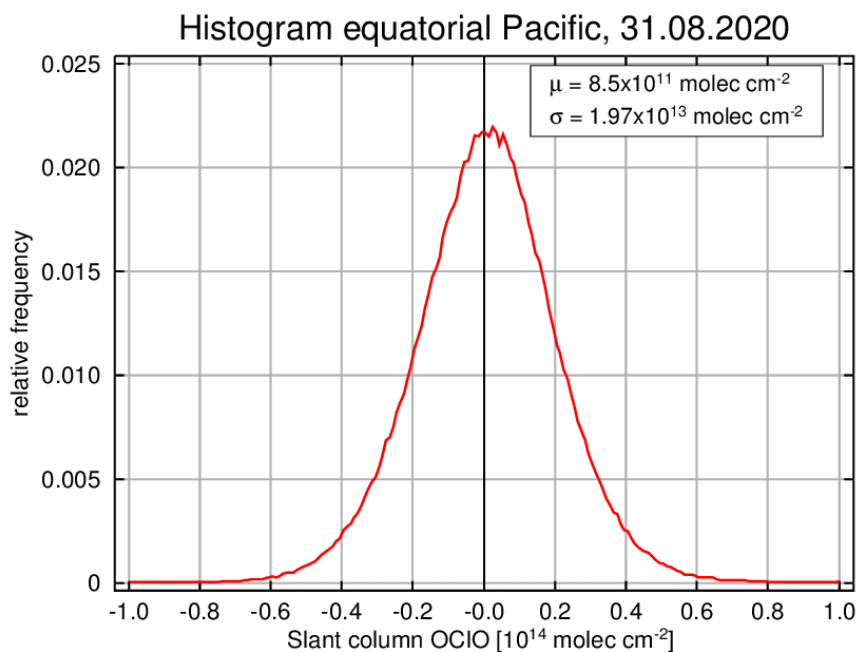
Figure 10.1: Scatter of OClO slant column densities in the equatorial Pacific (-15° <= latitude <= 15°, 160° <= longitude <= 220°). The box displays the mean (μ) and standard deviation (σ).

In order to investigate the stability of the precision over time, the scatter of values in the Pacific region was calculated for each day. With the exception of a few outliers, the scatter is nearly constant with a small seasonality, as shown as the red point in Figure 10.2. A remarkable feature is the sudden jump

to larger values in summer 2019, which can be explained by the decrease of the S5p ground pixel size (7 km to 5.5 km) on August 6, 2019.
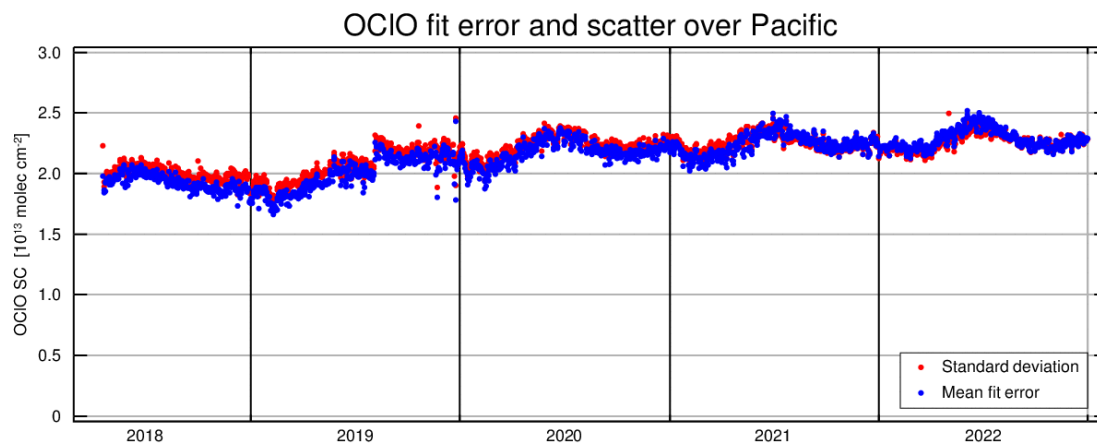
Figure 10.2: Scatter of the OClO slant column densities (standard deviation) over the equatorial Pacific (-15° <= Latitude <= 15°, 160° <= Longitude <= 220°) and the mean fit error in this region as a function of time.

The random uncertainty of the slant columns can also be directly estimated from the RMS of the fitting residual (Δ^2_{RMS}) and the diagonal elements of the covariance matrix $\mathbf{S}$, see equation 8-6. The square root of diagonal elements of $\mathbf{S}$ represents the error of the fit coefficient. The error of the chlorine dioxide fit coefficient is shown as the blue points in Figure 10.2. This approach assumes that the model is perfect in the sense that the linear superposition of the scaled cross-sections and the polynomial can fully describe the optical depth of the measurement. Any errors on the spectral shape of the cross-sections (for example from temperature dependence or imperfect knowledge of the slit function) will increase the residual and thus the estimate of the random uncertainty. Whether or not such a "model" error actually leads to an increased uncertainty in the slant column and by how much depends on the correlation between the spectral shape of the mismatch and all the cross-sections included in the DOAS retrieval. This random uncertainty is therefore an upper limit of the true random uncertainty. For the case of NO_2, it has been shown that the uncertainty retrieved from the fit is always larger than the random uncertainty estimated from the scatter of slant columns, but that for a good fit, these two quantities are very close (Zara et al., 2018).

Here, the uncertainty determined from the two methods gives very similar results. In the years 2018 and 2019, the fit error is often even smaller than the spread, which is likely related to the inclusion of the empirical cross-sections that compensate deficiencies in the fit. Over time, the fit error slightly increases, probably as result of instrument degradation. This seems, however, not to be reflected in the spread of values.
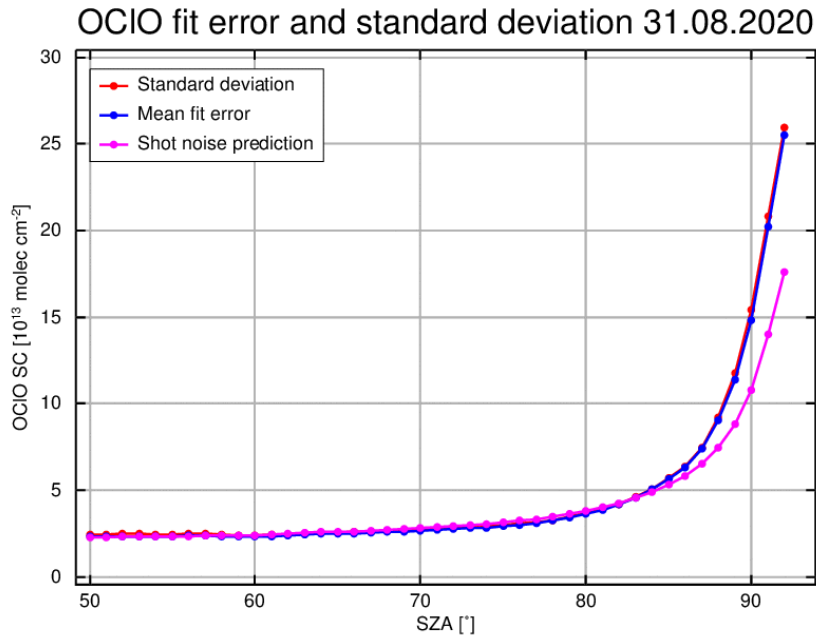
Figure 10.3: Solar zenith angle dependency of the scatter in OClO slant column on 31.08.2020. The pink line is a simple model estimate based on photon shot noise. See text for details.

Most applications use OClO columns at large SZA, where the estimates over the tropical region discussed so far do not apply. In order to evaluate the random noise at different SZA, all data in the NH were used for the test day 31.08.2020 and selected as function of solar zenith angle. The results are shown in Figure 10.3, again for the fitting error and the standard deviation of the OClO SCDs. As expected, the two quantities agree very well, indicating that the fit error is a good measure of the scatter also at large SZA. The scatter increases strongly with SZA, mainly because of the reduction in intensity and therefore an increase in photon shot noise. To evaluate the correlation between intensity and scatter of the OClO columns, a simple shot noise model calculation is also included in Figure 10.3. This assumes that the scatter $s(\Theta)$ of the OClO slant columns at SZA Θ can be written as

$$s(\Theta) = s(\Theta_0) \frac{\sqrt{\text{ints}(\Theta_0)}}{\sqrt{ints(\Theta)}}$$

10-1,

where Θ_0 is a reference SZA (50°) and $ints(\Theta)$ is the intensity measured at SZA Θ. As can be seen, this model leads to lower noise predictions at very large SZA than the analysis of the data, indicating that there are additional sources of error than just photon shot noise. The main result of this analysis is that the scatter in OClO slant columns increases with SZA from about 2×10^{13} molec cm^{-2} over the tropics to 15×10^{13} molec cm^{-2} at 90° SZA.

10.2 Uncertainties on destriping and bias correction

10.2.1 Destriping

As discussed in section 8.3, the spectral retrieval from imaging spectrometers may lead to row dependent offsets. Hence, a destriping is performed. Figure 10.4 shows the evolution of the destriping pattern from 2018 to 2022. In the retrieval, the stripe pattern is determined and applied on a daily basis. However, the pattern appears to be relatively stable over longer time periods with a small seasonality. Large changes occur when the version of the lv1 product changes. This could be related to the fact that the pseudo cross-sections were determined using data from 2019 and may be specific to the lv1 data version available at that time.
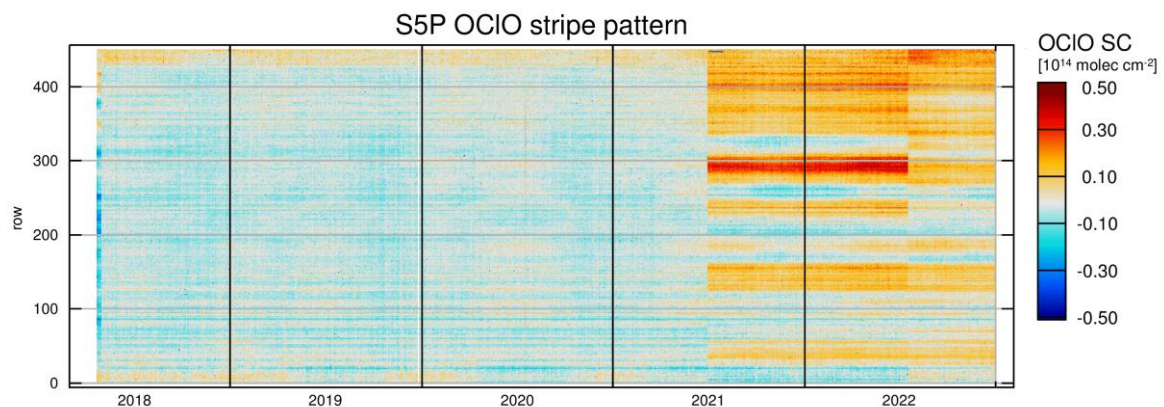
Figure 10.4: Evolution of the destriping pattern from 2018 to 2022. Changes in amplitude are linked to changes in the lv1 data version.

The peak magnitude of the destriping correction is 1×10^{13} molec cm^{-2} before July 2021 and 3×10^{13} molec cm^{-2} after that. This is the magnitude of bias that would be introduced for some viewing directions if no destriping were applied.

10.2.2 Bias correction

In general, two factors impact on the uncertainty of the bias correction: the error on the background column amount in the region for normalization, and differences in offset values between the region used for normalization and the actual scene. As chlorine dioxide is rapidly photolysed, the background column can confidently assumed to be zero in regions with small solar zenith angles. The second factor may have a larger impact, because the retrieval of chlorine dioxide may suffer from systematic differences in the retrieved column between land/ocean as well as cloudy/cloud-free scenes. In addition, there can be latitude (SZA) dependent biases that vary with season and are most pronounced at high latitudes. As chlorine dioxide is expected only at high latitudes in twilight conditions, the chlorine dioxide product cannot be easily corrected and may be affected by these scene specific biases. The impact of such bias problems is expected to be largely suppressed by adding the empirical cross-sections in the spectral retrieval. Figure 10.5 shows the mean chlorine dioxide slant column density over the equatorial Pacific ($-15° <= $ Latitude $<= 15°$, $160° <= $ Longitude $<= 220°$) as a function of time,

see also the histogram for a single day in Figure 10.1. The time series shows, that the bias determined in this region is approximately constant over time with values of about -2.5x10^{12} molec / cm^2. However, a seasonal dependency is observed which has a magnitude of about +-2.5x10^{12} molec / cm^2. The offset increases in summer 2021 and decreases again in summer 2022, in both cases because of changes in the lv1 data version. These changes are also visible in the time evolution of the destriping pattern in Figure 10.4.
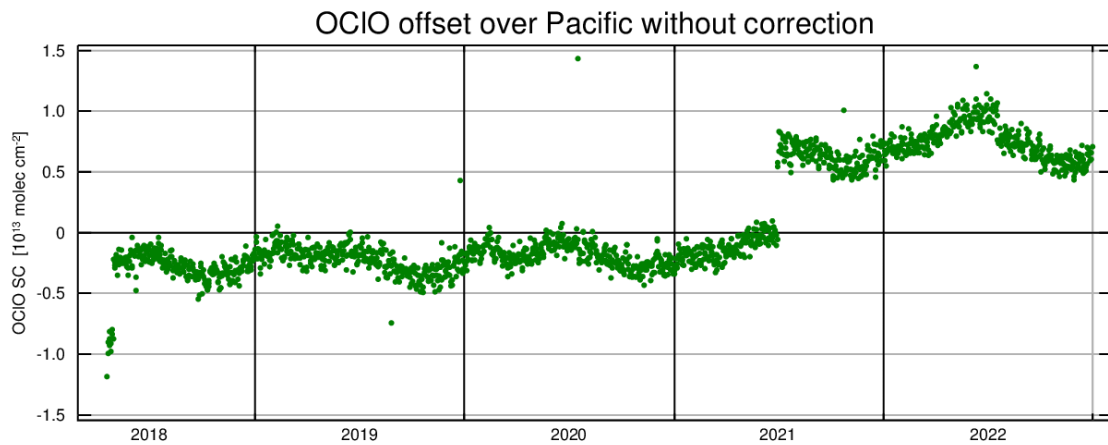
Figure 10.5: Mean chlorine dioxide slant column density over the equatorial Pacific (-15° <= latitude <= 15°, 160° <= longitude <= 220°) before offset correction.

Assuming an uncertainty of 100% on the temporal mean value in the equatorial Pacific, the uncertainty on the bias correction is estimated to be of the order of 5x10^{12} molec / cm^2.

10.3 Overall uncertainty

Making the assumption that the sources for the individual uncertainties are not correlated, the overall uncertainty $\sigma_{N_V}^2$ can be estimated through propagation of the individual error components.

$$\sigma_{N_V}^2 = \frac{1}{M^2}\left(\sigma_{N_S}^2 + \sigma_{N_{S,0}}^2 + \frac{N_S^2}{M^2}\sigma_M^2\right)$$ 10-2,

Where σ_{N_S}, $\sigma_{N_{S,0}}$, σ_M are the individual errors of the retrieved slant column, the destriping/bias correction and the air mass factor. For the slant columns provided in the current version of the OClO product, this reduces to

$$\sigma_{N_V}^2 = \sigma_{N_S}^2 + \sigma_{N_{S,0}}^2$$ 10-3,

10.4 Quality assurance (QA value)

In order to describe the quality of the retrieved OClO vertical column, and filter the observations, a quality assurance value (QA value) is assigned to each pixel. The QA value is a numerical value in the range [0 1], with the convention that a value <0.5 means that the pixel retrieval result should be

discarded. The QA value is not a continuous quantity, but use reduced in steps, if certain criteria are (not) fulfilled.

The following criteria are currently included

- Filter out descending part of orbit
- Filter by RMS scaled by square of measured intensity (see section 10.1 for justification)
- Filter by SZA range (only relevant for Polar chemistry)

The resulting QA values are listed in Table 10.1.

Table 10.1: Possible values of the QA value and their meaning

QA value	Meaning
0	Small SZA, High RMS, descending
0.1	Small SZA, High RMS, ascending
0.2	Large SZA, high RMS, descending
0.3	Large SZA, high RMS, ascending
0.5	Small SZA, low RMS, descending
0.6	Small SZA, low RMS, ascending
0.7	Large SZA, low RMS, descending
0.8	Large SZA, low RMS, ascending

11 Validation

11.1 Ground-based datasets

The main data source for validation are ground-based zenith-sky DOAS observations. Such measurements are performed in both hemispheres, and data from 8 stations is used. An overview on the data available is given in Table 11.1. While the overall coverage of this validation data set is limited, it provides a good sampling of different high latitude situations inside and outside of the Polar Vortex.

OClO data analysis of the ground-based stations is not harmonized, and some of the stations also suffer from time dependent offsets. This problem has been addressed by applying an objective offset correction, which clearly improved the consistency of the data set. Details on the data set and the data analysis can be found in the Validation Report [RD3].

A summary of the validation efforts for the ground-based sites is displayed in Figure 11.1. It shows a scatter plot of OClO SCD derived using the S5p algorithm vs. OClO SCDs from all ground-based sites, as well as absolute biases between the satellite and ground-based products. There is generally an excellent agreement between the satellite and ground-based datasets with a high correlation and a slope close to one. An in depth analysis can be found in the Validation Report [RD3].

Table 11.1: Overview on ground-based datasets available.

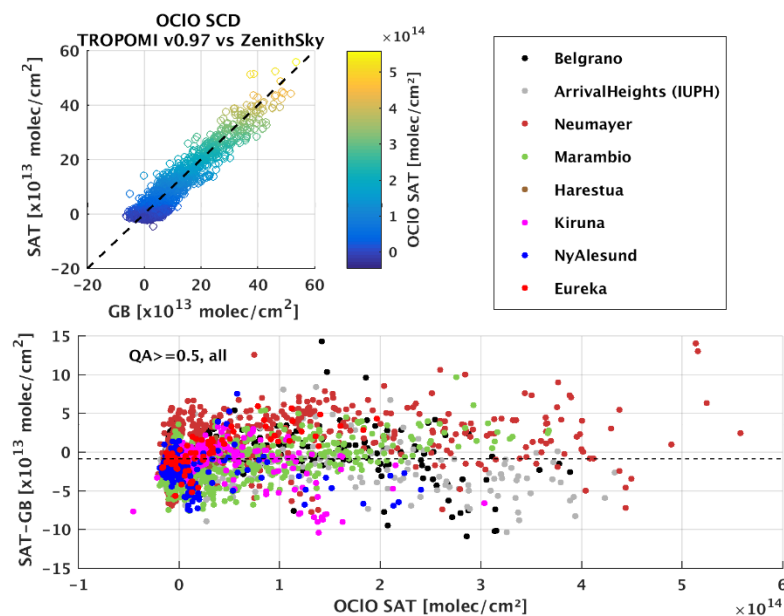| Location	Latitude	Data Provider	Time Coverage
Eureka	80° N	UToronto	2006-present
Ny-Ålesund	78.9° N	IUP-UB	1995-present
Kiruna	67.8° N	MPIC	1997-present
Harestua	60.2° N	BIRA-IASB	2012-present
Marambio	64.2° S	INTA	2015-present
Neumayer	70.6° S	IUP-UH	2006-present
Arrival Heights	77.7° S	IUP-UH and NIWA	2006-present 2007-2017 (NIWA)
Belgrano	77.8° S	INTA	2011; 2015-present

Figure 11.1: Scatter plot and absolute bias as a function of the TROPOMI OClO SCD, for bias corrected ground-based sites.

11.2 Satellite datasets

In order to increase the number of data points used for verification / validation, and also in order to assess the usefulness of the S5p OClO product to extend the existing satellite record of OClO

observations, comparisons will be made with OClO slant columns retrieved from other satellite instruments. In terms of observation geometry and overpass time, OMI data is the most appropriate data set for comparison. However, due to the row anomaly, OMI coverage and data quality is reduced.

Figure 11.2 shows time series of chlorine dioxide slant column densities retrieved from S5p and OMI respectively at 90° solar zenith angle. It has to be noted that not the operational OMI OClO product is used, but an independent data product developed by IUP-UB in which a hemisphere specific bias correction was applied. The time series shows very good consistency between the two data products, albeit the OMI data is much noisier and has a negative bias in the SH in summer. Both instruments capture the seasonality and the inter-annual differences of the chlorine activation periods in a very similar way.
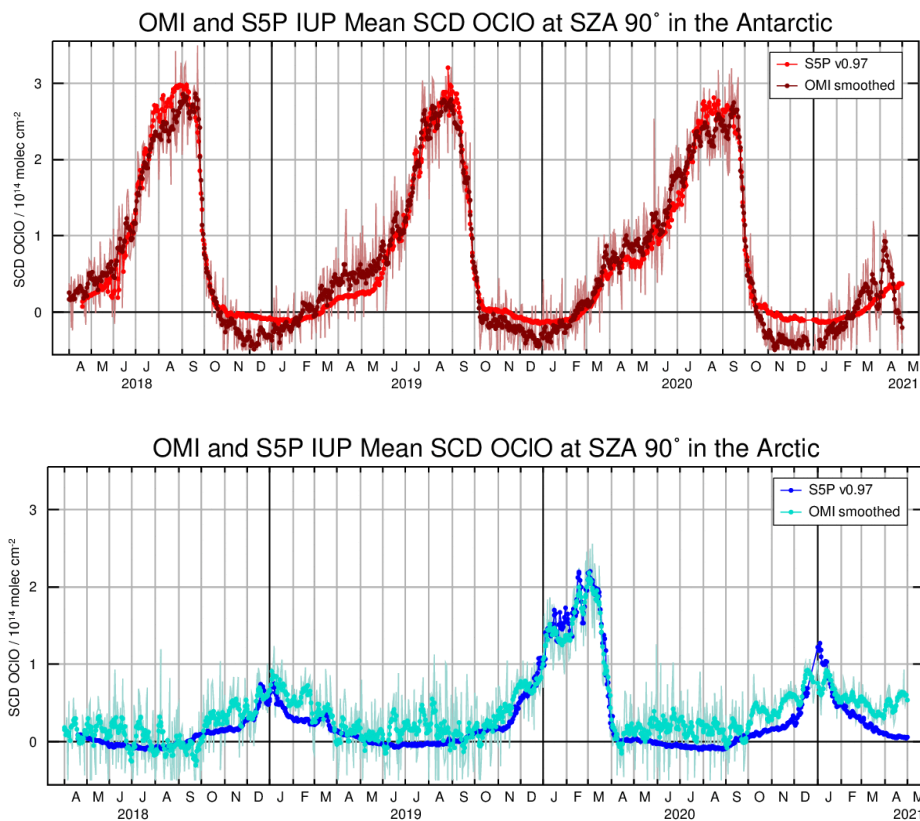
Figure 11.2: Comparison between OClO columns from S5p and OMI for the SH (top) and the NH (bottom). All data are sampled at 90° SZA. OMI data have been offset corrected and smoothed over 7 days for clarity (see text for details). The unsmoothed data are shown as thin line in the background.

As a secondary comparison product, OClO columns from GOME2 will also be used. However, as the overpass time of the MetOP satellites is different to that of S5p, no direct comparison will be possible, and mainly qualitative comparisons will be performed, for example on inter-annual variations and spatial patterns.

12 Conclusions and Outlook

This document presents the baseline approach for the retrieval of chlorine dioxide from TROPOMI aboard Sentinel-5p. The retrieval builds on the heritage of previous satellite missions, such as GOME, SCIAMACHY, GOME-2 and OMI. The algorithm uses a standard DOAS approach to retrieve slant column densities of chlorine monoxide from radiance spectra and daily irradiances in the UV spectral range. Similar to previous sensors, the spectral retrieval of chlorine dioxide from S5p suffers from biases. The algorithm developed makes use of several empirical cross-sections derived from averaged DOAS fitting residuals to minimize the bias.

The algorithm applies destriping and offset corrections over the equatorial Pacific in order to reduce across-track striping inherent to push-broom sensors and to correct for remaining bias despite the inclusion of empirical cross-sections. Evaluation of the first 5 years of TROPOMI data shows, that offsets and stripes change whenever the lv1 version changes, but the resulting product remains of nearly constant quality throughout the time series.

The random uncertainty reported in the fitting errors is compared to the scatter of the OClO slant columns over regions expected to show no chlorine activation. The agreement between these two quantities is excellent, indicating a) a good fit and b) the applicability of the fitting error as uncertainty estimate. Uncertainties are of the order of 2×10^{13} molec cm^{-2} in tropical regions and increase to about 15×10^{13} molec cm^{-2} at 90° SZA. The increase in uncertainty with SZA is qualitatively in line with the expected increase from reduced intensity.

In terms of feasibility, the computational load of this product is low and the output file size of about 250 MB is similar to other S5p lv2 products.

Comparison of the TROPOMI OClO product to other satellite data sets shows high signal to noise, small biases and good agreement. Validation with ground based data from high latitude stations shows excellent agreement.

For future versions of the TROPOMI OClO product, several improvements and extensions are envisaged:

1. Reprocessing of the full data set with a consistent lv1 data version
2. Improvement of bias-correction in particular at large SZA without chlorine activation
3. Addition of AMF and vertical columns
4. Full implementation of meta data in the S5P netCDF file format

13 References

Aliwell, S. R., Roozendael, M. V., Johnston, P. V., Richter, A., Wagner, T., Arlander, D. W., Burrows, J. P., Fish, D. J., Jones, R. L., Tørnkvist, K. K., Lambert, J.-C., Pfeilsticker, K. and Pundt, I.: Analysis for BrO in zenith-sky spectra: An intercomparison exercise for analysis improvement, J. Geophys. Res. Atmospheres, 107(D14), doi:10.1029/2001JD000329, 2002.

Beirle, S., Sihler, H. and Wagner, T.: Linearisation of the effects of spectral shift and stretch in DOAS analysis, Atmospheric Meas. Tech., 6(3), 661–675, doi:https://doi.org/10.5194/amt-6-661-2013, 2013.

Boersma, K. F., Eskes, H. J. and Brinksma, E. J.: Error analysis for tropospheric NO2 retrieval from space, J. Geophys. Res. Atmospheres, 109(D4), doi:10.1029/2003JD003962, 2004.

Burrows, J. P., Weber, M., Buchwitz, M., Rozanov, V., Ladstätter-Weißenmayer, A., Richter, A., DeBeek, R., Hoogen, R., Bramstedt, K., Eichmann, K.-U., Eisinger, M. and Perner, D.: The Global Ozone Monitoring Experiment (GOME): Mission Concept and First Scientific Results, J. Atmospheric Sci., 56(2), 151–175, doi:10.1175/1520-0469(1999)056<0151:TGOMEG>2.0.CO;2, 1999.

Chance, K. and Kurucz, R. L.: An improved high-resolution solar reference spectrum for earth's atmosphere measurements in the ultraviolet, visible, and near infrared, J. Quant. Spectrosc. Radiat. Transf., 111(9), 1289–1295, doi:10.1016/j.jqsrt.2010.01.036, 2010.

Fish, D. J. and Jones, R. L.: Rotational Raman scattering and the ring effect in zenith-sky spectra, Geophys. Res. Lett., 22(7), 811–814, doi:10.1029/95GL00392, 1995.

Fussen, D., Vanhellemont, F., Dodion, J., Bingen, C., Mateshvili, N., Daerden, F., Fonteyn, D., Errera, Q., Chabrillat, S., Kyrölä, E., Tamminen, J., Sofieva, V., Hauchecorne, A., Dalaudier, F., Bertaux, J.-L., Renard, J.-B., Fraisse, R., d'Andon, O. F., Barrot, G., Guirlet, M., Mangin, A., Fehr, T., Snoeij, P. and Saavedra, L.: A global OClO stratospheric layer discovered in GOMOS stellar occultation measurements, Geophys. Res. Lett., 33(13), doi:10.1029/2006GL026406, 2006.

General, S., Bobrowski, N., Pöhler, D., Weber, K., Fischer, C. and Platt, U.: Airborne I-DOAS measurements at Mt. Etna: BrO and OClO evolution in the plume, J. Volcanol. Geotherm. Res., 300, 175–186, doi:10.1016/j.jvolgeores.2014.05.012, 2015.

Gil, M., Puentedura, O., Yela, M., Parrondo, C., Jadhav, D. B. and Thorkelsson, B.: OClO, NO2 and O3 total column observations over Iceland during the winter 1993/94, Geophys. Res. Lett., 23(23), 3337–3340, doi:10.1029/96GL03102, 1996.

Krecl, P., Haley, C. S., Stegman, J., Brohede, S. M. and Berthet, G.: Retrieving the vertical distribution of stratospheric OClO from Odin/OSIRIS limb-scattered sunlight measurements, Atmospheric Chem. Phys., 6(7), 1879–1894, doi:https://doi.org/10.5194/acp-6-1879-2006, 2006.

Kreher, K., Keys, J. G., Johnston, P. V., Platt, U. and Liu, X.: Ground-based measurements of OClO and HCl in austral spring 1993 at Arrival Heights, Antarctica, Geophys. Res. Lett., 23(12), 1545–1548, doi:10.1029/96GL01318, 1996.

Kromminga, H., Orphal, J., Spietz, P., Voigt, S. and Burrows, J. P.: New measurements of OClO absorption cross-sections in the 325–435 nm region and their temperature dependence between 213

and 293 K, J. Photochem. Photobiol. Chem., 157(2), 149–160, doi:10.1016/S1010-6030(03)00071-6, 2003.

Kühl, S., Pukite, J., Deutschmann, T., Platt, U. and Wagner, T.: SCIAMACHY limb measurements of NO2, BrO and OClO. Retrieval of vertical profiles: Algorithm, first results, sensitivity and comparison studies, Adv. Space Res., 42(10), 1747–1764, doi:10.1016/j.asr.2007.10.022, 2008.

Noël, S., Bramstedt, K., Bovensmann, H., Gerilowski, K., Burrows, J. P., Standfuss, C., Dufour, E. and Veihelmann, B.: Quantification and mitigation of the impact of scene inhomogeneity on Sentinel-4 UVN UV-VIS retrievals, Atmos Meas Tech, 5(6), 1319–1331, doi:10.5194/amt-5-1319-2012, 2012.

Oetjen, H., Wittrock, F., Richter, A., Chipperfield, M. P., Medeke, T., Sheode, N., Sinnhuber, B.-M., Sinnhuber, M. and Burrows, J. P.: Evaluation of stratospheric chlorine chemistry for the Arctic spring 2005 using modelled and measured OClO column densities, Atmospheric Chem. Phys., 11(2), 689–703, doi:https://doi.org/10.5194/acp-11-689-2011, 2011.

Pommereau, J.-P. and Piquard, J.: Observations of the vertical distribution of stratospheric OClO, Geophys. Res. Lett., 21(13), 1231–1234, doi:10.1029/94GL00390, 1994.

Puķīte, J. and Wagner, T.: Quantification and parametrization of non-linearity effects by higher-order sensitivity terms in scattered light differential optical absorption spectroscopy, Atmospheric Meas. Tech., 9(5), 2147–2177, doi:https://doi.org/10.5194/amt-9-2147-2016, 2016.

Puķīte, J., Borger, C., Dörner, S., Gu, M., Frieß, U., Meier, A. C., Enell, C.-F., Raffalski, U., Richter, A. and Wagner, T.: Retrieval algorithm for OClO from TROPOMI (TROPOspheric Monitoring Instrument) by differential optical absorption spectroscopy, Atmos. Meas. Tech., 14(12), 7595–7625, doi:10.5194/amt-14-7595-2021, 2021.

Renard, J. B., Lefevre, F., Pirre, M., Robert, C. and Huguenin, D.: Vertical Profile of Night-Time Stratospheric OClO, J. Atmospheric Chem., 26(1), 65–76, doi:10.1023/A:1005757321761, 1997.

Richter, A., Eisinger, M., Ladstätter-weißenmayer, A. and Burrows, J. P.: DOAS Zenith Sky Observations: 2. Seasonal Variation of BrO Over Bremen (53°N) 1994-1995, J. Atmospheric Chem., 32(1), 83–99, doi:10.1023/A:1006077725894, 1999.

Richter, A., Wittrock, F., Weber, M., Beirle, S., Kühl, S., Platt, U., Wagner, T., Wilms-Grabe, W. and Burrows, J. P.: GOME Observations of Stratospheric Trace Gas Distributions during the Splitting Vortex Event in the Antarctic Winter of 2002. Part I: Measurements, J. Atmospheric Sci., 62(3), 778–785, doi:10.1175/JAS-3325.1, 2005.

Richter, A., Slijkhuis, S. and Loyola, D.: Offline Total OClO validation report, Validation Report, EUMETSAT. [online] Available from: http://www.iup.uni-bremen.de/doas/reports/o3saf_vs_gome-2_oclo_finalreport_091208.pdf, 2009.

Richter, A., Begoin, M., Hilboll, A. and Burrows, J. P.: An improved NO$_2$ retrieval for the GOME-2 satellite instrument, Atmospheric Meas. Tech., 4(6), 1147–1159, doi:10.5194/amt-4-1147-2011, 2011.

Richter, A., Wittrock, F. and Valks, P.: Evaluation of the possibility to derive reliable OClO slant columns from GOME2b and GOME2a spectra, Final Report, EUMETSAT. [online] Available from: http://www.iup.uni-bremen.de/doas/reports/o3m-saf_oclo_2_report_160427.pdf, 2016.

Richter, A., Hilboll, A., Sanders, A., Burrows, J.P., Inhomogeneous scene effects in OMI NO2 observations, EGU General Assembly, Vienna, Austria, April 2018. [online] Available from: http://www.iup.uni-bremen.de/doas/posters/egu_2018_richter.pdf, 2018.

Rigby, M., Park, S., Saito, T., Western, L. M., Redington, A. L., Fang, X., Henne, S., Manning, A. J., Prinn, R. G., Dutton, G. S., Fraser, P. J., Ganesan, A. L., Hall, B. D., Harth, C. M., Kim, J., Kim, K.-R., Krummel, P. B., Lee, T., Li, S., Liang, Q., Lunt, M. F., Montzka, S. A., Mühle, J., O'Doherty, S., Park, M.-K., Reimann, S., Salameh, P. K., Simmonds, P., Tunnicliffe, R. L., Weiss, R. F., Yokouchi, Y. and Young, D.: Increase in CFC-11 emissions from eastern China based on atmospheric observations, Nature, 569(7757), 546–550, doi:10.1038/s41586-019-1193-4, 2019.

Roscoe, H. K., Hill, J. G. T., Jones, A. E. and Sarkissian, A.: Improvements to the accuracy of zenith-sky measurements of total ozone by visible spectrometers II: use of daily air-mass factors, J. Quant. Spectrosc. Radiat. Transf., 68(3), 327–336, doi:10.1016/S0022-4073(00)00057-1, 2001.

Schiller, C., Wahner, A., Platt, U., Dorn, H.-P., Callies, J. and Ehhalt, D. H.: Near UV atmospheric absorption measurements of column abundances during Airborne Arctic Stratospheric Expedition, January – February 1989: 2. OClO observations, Geophys. Res. Lett., 17(4), 501–504, doi:10.1029/GL017i004p00501, 1990.

Seo, S., Richter, A., Blechschmidt, A.-M., Bougoudis, I., and Burrows, J. P.: First high-resolution BrO column retrievals from TROPOMI, Atmos. Meas. Tech., 12, 2913-2932, https://doi.org/10.5194/amt-12-2913-2019, 2019.

Serdyuchenko, A., Gorshelev, V., Weber, M., Chehade, W. and Burrows, J. P.: High spectral resolution ozone absorption cross-sections – Part 2: Temperature dependence, Atmos Meas Tech, 7(2), 625–636, doi:10.5194/amt-7-625-2014, 2014.

Solomon, S., Schmeltekopf, A. L. and Sanders, R. W.: On the interpretation of zenith sky absorption measurements, J. Geophys. Res. Atmospheres, 92(D7), 8311–8319, doi:10.1029/JD092iD07p08311, 1987.

Solomon, S., Mount, G. H., Sanders, R. W., Jakoubek, R. O. and Schmeltekopf, A. L.: Observations of the Nighttime Abundance of OClO in the Winter Stratosphere Above Thule, Greenland, Science, 242(4878), 550–555, doi:10.1126/science.242.4878.550, 1988.

Thalman, R. and Volkamer, R.: Temperature dependent absorption cross-sections of O_2–O_2 collision pairs between 340 and 630 nm and at atmospherically relevant pressure, Phys. Chem. Chem. Phys., 15(37), 15371–15381, doi:10.1039/C3CP50968K, 2013.

Theys, N., Smedt, I. D., Roozendael, M. V., Froidevaux, L., Clarisse, L. and Hendrick, F.: First satellite detection of volcanic OClO after the eruption of Puyehue-Cordón Caulle, Geophys. Res. Lett., 41(2), 667–672, doi:10.1002/2013GL058416, 2014.

Tørnkvist, K. K., Arlander, D. W. and Sinnhuber, B.-M.: Ground-Based UV Measurements of BrO and OClO over Ny-Ålesund during Winter 1996 and 1997 and Andøya during Winter 1998/99, J. Atmospheric Chem., 43(2), 75–106, doi:10.1023/A:1019905006390, 2002.

Valks, P., Loyola, D., Hao, N., Hedelt, P., Slijkhuis, S., Grossi, M., Gimeno Garcia, S. and Lutz, R.: ATBD GOME-2 Total Column Products of Ozone, NO2, BrO, HCHO, SO2, H2O, OClO and Cloud Properties, ATBD, EUMETSAT. [online] Available from: https://acsaf.org/docs/atbd/Algorithm_Theoretical_Basis_Document_NTO_OTO_DR_GDP48_Jun_2017.pdf (Accessed 28 February 2020), 2017.

Vandaele, A. C., Hermans, C., Simon, P. C., Carleer, M., Colin, R., Fally, S., Merienne, M. F., Jenouvrier, A. and Coquart, B.: Measurements of the NO_2 absorption cross-section from 42000 cm^{-1} to 10 000 cm^{-1} (238-1000 nm) at 220 K and 294 K, J. Quant. Spectrosc. Radiat. Transf., 59(3–5), 171–184, doi:10.1016/S0022-4073(97)00168-4, 1998.

Veefkind, J. P., Aben, I., McMullan, K., Förster, H., de Vries, J., Otter, G., Claas, J., Eskes, H. J., de Haan, J. F., Kleipool, Q., van Weele, M., Hasekamp, O., Hoogeveen, R., Landgraf, J., Snel, R., Tol, P., Ingmann, P., Voors, R., Kruizinga, B., Vink, R., Visser, H. and Levelt, P. F.: TROPOMI on the ESA Sentinel-5 Precursor: A GMES mission for global observations of the atmospheric composition for climate, air quality and ozone layer applications, Remote Sens. Environ., 120, 70–83, doi:10.1016/j.rse.2011.09.027, 2012.

Vountas, M., Rozanov, V. V. and Burrows, J. P.: RING EFFECT: Impact of rotational Raman scattering on radiative transfer in Earth's atmosphere, J. Quant. Spectrosc. Radiat. Transf., 60(6), 943–961, doi:10.1016/S0022-4073(97)00186-6, 1998.

Vountas, M., Richter, A., Wittrock, F. and Burrows, J. P.: Inelastic scattering in ocean water and its impact on trace gas retrievals from satellite data, Atmos Chem Phys, 3(5), 1365–1375, doi:10.5194/acp-3-1365-2003, 2003.

Wagner, T., Leue, C., Pfeilsticker, K. and Platt, U.: Monitoring of the stratospheric chlorine activation by Global Ozone Monitoring Experiment (GOME) OClO measurements in the austral and boreal winters 1995 through 1999, J. Geophys. Res. Atmospheres, 106(D5), 4971–4986, doi:10.1029/2000JD900458, 2001.

Wagner, T., Wittrock, F., Richter, A., Wenig, M., Burrows, J. P. and Platt, U.: Continuous monitoring of the high and persistent chlorine activation during the Arctic winter 1999/2000 by the GOME instrument on ERS-2, J. Geophys. Res. Atmospheres, 107(D20), doi:10.1029/2001JD000466, 2002.

Wilmouth, D.M., Hanisco, T.F., Donahue, N.M., Anderson J.G. (1999), Fourier Transform Ultraviolet Spectroscopy of the $A^2\Pi_{3/2} \leftarrow X^2\Pi_{3/2}$ Transition of BrO, J. Phys. Chem, 103, doi:10.1021/jp991651o

Zara, M., Boersma, K. F., De Smedt, I., Richter, A., Peters, E., van Geffen, J. H. G. M., Beirle, S., Wagner, T., Van Roozendael, M., Marchenko, S., Lamsal, L. N. and Eskes, H. J.: Improved slant column density retrieval of nitrogen dioxide and formaldehyde for OMI and GOME-2A from QA4ECV: intercomparison, uncertainty characterisation, and trends, Atmospheric Meas. Tech., 11(7), 4033–4058, doi:https://doi.org/10.5194/amt-11-4033-2018, 2018.

A. PRODUCT FILE FORMAT

Table 13.1: List of variables included in the TROPOMI OClO product. The second column indicates the group of the file content structure in which the variable is stored.

Name	Group	Units	Description / long name
time	PRODUCT	s	Reference time since 1995-01-01 00:00:00
delta_time	PRODUCT	ms	Time difference with respect to the reference time variable for each scanline.
time_utc	PRODUCT	-	String array with each observation time stored as an ISO date string
chlorinedioxide_slant_column_density	PRODUCT	molec. cm^{-2}	OClO slant column
chlorinedioxide_slant_column_density _precision	PRODUCT	molec. cm^{-2}	OClO slant column random error
qa_value	PRODUCT	1	Quality assurance value describing the quality of the measurement. It is recommended to reject all pixels with a qa_value less than 0.5
latitude	PRODUCT	degree north	Latitude of the centre of each ground pixel
longitude	PRODUCT	degree east	Longitude of the centre of each ground pixel
solar_zenith_angle	GEOLOCATIONS	degree	Zenith angle of the sun at the ground pixel location
viewing_zenith_angle	GEOLOCATIONS	degree	Zenith angle of the satellite measured at the ground pixel location
relative_azimuth_angle	GEOLOCATIONS	degree	Relative azimuth angle between the solar azimuth and the viewing azimuth of the satellite measured at the ground pixel location
latitude_bounds	GEOLOCATIONS	degree north	The four latitude boundaries of each ground pixel.
longitude_bounds	GEOLOCATIONS	degree east	The four longitude boundaries of each ground pixel.
brominemonoxide_slant_column_density	DETAILED_RESULTS	molec cm^{-2}	BrO slant column
brominemonoxide_slant_column_density_precision	DETAILED_RESULTS	molec cm^{-2}	BrO slant column random error
nitrogendioxide_slant_column_density	DETAILED_RESULTS	molec cm^{-2}	NO2 slant column
nitrogendioxide_slant_column_density_precision	DETAILED_RESULTS	molec cm^{-2}	NO2 slant column random error
ozone_223K_slant_column_density	DETAILED_RESULTS	molec cm^{-2}	O3 @ 223K slant column
ozone_223K_slant_column_density_precision	DETAILED_RESULTS	molec cm^{-2}	O3 @ 223K slant column random error
ozone_243K_slant_column_density	DETAILED_RESULTS	molec cm^{-2}	O3 @ 243K slant column
ozone_243K_slant_column_density_precision	DETAILED_RESULTS	molec cm^{-2}	O3 @ 243K slant column random error

oxygen_oxygen_dimer_slant_column_density	DETAILED_RESULTS	molec^2 cm^{-5}	O2-O2 slant column divided by 1x1040
oxygen_oxygen_dimer_slant_column_density_precision	DETAILED_RESULTS	molec^2 cm^{-5}	O2-O2 slant column random error divided by 1x1040
ring_coefficient	DETAILED_RESULTS	1	Fitting factor for Ring effect
ring_coefficient _precision	DETAILED_RESULTS	1	Random error of Ring effect coefficient
intensity_offset_coefficient	DETAILED_RESULTS	1	Fitting factor for intensity offset
intensity_offset_coefficient _precision	DETAILED_RESULTS	1	Random error of intensity offset coefficient
intensity_slope_coefficient	DETAILED_RESULTS	1	Fitting factor for intensity slope
intensity_slope_coefficient _precision	DETAILED_RESULTS	1	Random error of intensity slope coefficient
residual_inhomo_positive_coefficient	DETAILED_RESULTS	1	Fitting factor for inhomogeneity positive shift residual
residual_inhomo_positive_coefficient _precision	DETAILED_RESULTS	1	Random error of inhomogeneity positive shift residual coefficient
residual_inhomo_negative_coefficient	DETAILED_RESULTS	1	Fitting factor for inhomogeneity negative shift residual
residual_inhomo_negative_coefficient _precision	DETAILED_RESULTS	1	Random error of inhomogeneity negative shift residual coefficient
residual_nh_coefficient	DETAILED_RESULTS	1	Fitting factor for northern hemisphere residual
residual_nh_coefficient _precision	DETAILED_RESULTS	1	Random error of northern hemisphere residual coefficient
residual_tropics_coefficient	DETAILED_RESULTS	1	Fitting factor for tropical residual
residual_tropics_coefficient _precision	DETAILED_RESULTS	1	Random error of tropical residual coefficient
rms_fit	DETAILED_RESULTS	1	Root mean Square of the residual
wavelength_calibration_offset	DETAILED_RESULTS	nm	Wavelength offset applied
wavelength_calibration_stretch	DETAILED_RESULTS	1	Wavelength stretch applied
cloud_fraction_crb	INPUT_DATA	1	Cloud fraction from NO2 OFFL product
cloud_pressure_crb	INPUT_DATA	hPa	Cloud pressure from NO2 OFFL product
ecmwf_pv_50mbar	INPUT_DATA	K m^2 kg^{-1} s^{-1}	ECMWF potential vorticity at 50 mbar level
ground_pixel_quality_flag	INPUT_DATA	1	Ground pixel quality flag from lv1 file